University of Crete, Department of Physics

FO.R.T.H., Institute of Electronic Structure and Lasers

MSc Thesis

Optimization and characterization of highly elliptical XUV radiation

Spachis Leandros

Supervisors

Dr. Tzallas Paraskevas

Prof. emer. Charalambidis Dimitris

Prof. Rakitzis Theodore-Peter

Heraklion, May 2022

Acknowledgements

I would like to thank my supervisor Dr. Tzallas who gave me the opportunity to participate in front line research in attosecond science. I am very grateful to Dr E. Skantzakis for his continuous support and patience during by MSc thesis research. I would also like to thank Mr E. Vassakis, Mr T. Lambrou, Dr I. Orfanos, Dr I Liontos and Dr. V. Tsafas, for useful discussions and assistance in various matters regarding the experimental apparatus and data analysis. Finally, I would like to extend my sincere thanks to Prof. emer. Charalambidis and Prof. Rakitzis, members of my MSc thesis committee.

Abstract

The purpose of this thesis is the experimental study of the generation of highly elliptically polarized XUV light, produced through the non-linear process of high-order harmonic generation, via the interaction of a femtosecond infrared (IR) bicircular (at 800nm and 400nm) laser field with Argon gas. The bi-circular filed was produced using a MAZEL-TOV-like (Mach-Zehnder-Less for Threefold Optical Virginia spiderwort-like) device, a crucial component of which is a BBO crystal. This process can lead to the production of table-top sources of XUV light with circular/elliptical polarization and ultrashort time duration (from tens of femtoseconds to hundreds of attoseconds), which can be utilized to further our understanding of the structural, electronic and magnetic properties of matter. The first aim of the work presented here is the spectroscopic characterization of the high harmonics generated and the study of the changes introduced in the spectra by different rotation angles of the BBO crystal, leading to the optimization of the produced XUV ellipticity. The second aim is the characterization of the polarization state of the generated high harmonics, and the confirmation of the presence and stability of high ellipticity. Both experiments were conducted in the "Attosecond Science and Technology" laboratory at the Institute for Electronic Structure and Lasers (at FORTH), using the MW line driven by the Ti-Sapphire pulsed laser, with carrier wavelength of 800nm, pulse duration of 25fs and energy up to 400mJ per pulse. The spectral characterization was achieved using a Time-of-Flight spectrometer, while the polarization state was studied using a reflective polarimeter and a grating spectrometer.

Table of contents

1. Introduction

The purpose of this thesis is the experimental study of the generation of (XUV) light with circular or elliptical polarization, produced through the non-linear process of high-order harmonic generation, specifically from the interaction of femtosecond infrared (IR) bicircular laser field with noble gases (in this case Argon is used). This laser-matter interaction can lead to the production of table-top sources of XUV light with circular polarization and ultrashort time duration (from tens of femtoseconds to hundreds of attoseconds), which can be applied as an important tool to the further study of the structural, electronic and magnetic properties of matter. In general, the developed beamline can also enable the generation of energetic and coherent XUV pulses, with energies up to 100nJ per pulse. Optimization and characterization of the helicity and ellipticity of the generated pulses is the ultimate purpose of this effort.

High-order harmonic generation (HHG) is one of the most varied and dynamic parts of strong-field physics, which arose over the past two to three decades from a number of advances in physics and technology, involving mainly photonics. The invention of laser by Maiman in 1960 (Maiman 1960) opened the way for the investigation of laser-matter interactions, especially after the development of the chirped pulse amplification technique by Strickland and Mourou a couple of decades later in (Strickland & Mourou 1985). Thanks to this breakthrough in the laser technology, laser intensities achieved keep rising, reaching 10^{22} W/cm^2 (Yanovsky et al. 2008), or recently even higher values by at least two orders of magnitude.

This bright coherent light source has laid the foundations for the construction of a new field in optics, *non-linear optics*, while it also strongly affected atomic physics, giving rise to laser spectroscopy. A significant improvement in the non-linear optics field and atomic physics has been realized because laser field intensities were enhanced and reached the value of the Coulomb field acting on the bound electron in an atom. One of the physical processes revealed as a result of the interaction between the strong laser filed and the atom, is the HHG, mentioned above. It was discovered in 1987 (McPherson et al., 1987; Ferray et al., 1988), via the interaction of a rare gas with a laser field which resulted in the generation of odd multiples of the laser frequency. In 1993 Corkum (Corkum 1993) introduced the three step model, a theoretical framework to explain semi-classically the generation of higher harmonics. Full quantum mechanical approaches have also been developed since. On the experimental front, the first experiments produced linearly polarized harmonics. The experimental production of circular/highly elliptical harmonics (which is of interest in the present thesis) and their polarization control, have been the subject of several studies applying different experimental approaches, such as the use of non collinear geometry for the generation of higher energy photons (Hickstein et al. 2015), resonant HHG in elliptical fields (Ferré et al. 2015, Skantzakis et al. 2016), the combination of two driving fields, a strong and a weak one to generate elliptically polarized harmonics with fully controllable ellipticity (Fleischer et al. 2013), polarimetry with two orthogonally polarized laser fields (Lambert, et al. 2015), bichromatic counter-rotating circularly polarized fields (Long, S. et al. 1995, Milošević et al. 2000, Milošević & Becker 2000) or co-rotating bi-circularly polarized laser fields.

In the present thesis, we study the production of coherent XUV radiation of high ellipticity through the generation of high harmonics from the interaction of a bicircular two-frequency laser field (at 800nm and 400nm) with Argon gas. The specific aim of the experiment is the

characterization and optimization of the produced highly elliptical XUV radiation by introducing different angles to the BBO crystal**.**

The structure of the thesis is as follows: Section 2 describes the theoretical background and the models used to explain the HHG (either linearly or elliptically polarized). Section 3 describes the experiments conducted including the experimental setup and the data obtained. Section 4 describes briefly the data analysis, and in Section 5 we discuss the interpretation of the results. Section 6 summarizes the conclusions of the present work.

2. Theoretical background

2.1. Ionization by laser fields in the Strong Field regime

The key process that triggers most phenomena observed in strong laser fields, including high harmonic generation, is ionization. In the strong field regime, the laser intensities are higher than 10^{13} W/cm^2, although ionization of the atom can also happen at lower intensities. What happens in the strong field regime, where the laser field is comparable to the electric field at the first Bohr orbit, is that the atomic potential is affected by the high field strength that acts on the atom. The external (laser) field cannot be considered as a perturbation, but needs to be considered as an integral part of the dynamics of the motion of the electron. In order for the laser peak intensity to reach the value of the electric field of $E_{Bohr} \sim 5 \times 10^{11}$ V/m, the laser intensity has to be equal to $I = 3.5 \times 10^{16}$ W/cm^2. However, multiphoton processes and bending of the binding potential can take place at intensities that are lower than the above value by a factor of 100 or more. The mechanisms that cause ionization of atoms by strong fields will be briefly presented in the following paragraphs. Depending on the relation between the laser intensity and the strength of the atomic potential, the ionization mechanisms can be classified into three types: *multi-photon ionization (MPI)*, which occurs for laser intensities up to $10^{12} - 10^{13}$ W/cm^2, *tunnel ionization (TI)*, for laser intensities $10^{14} - 10^{15}$ W/cm^2 and *over the barrier ionization (OTBI)*, for intensities above 10^{15} W/cm^2 (Frank 2011, Popov 2004).

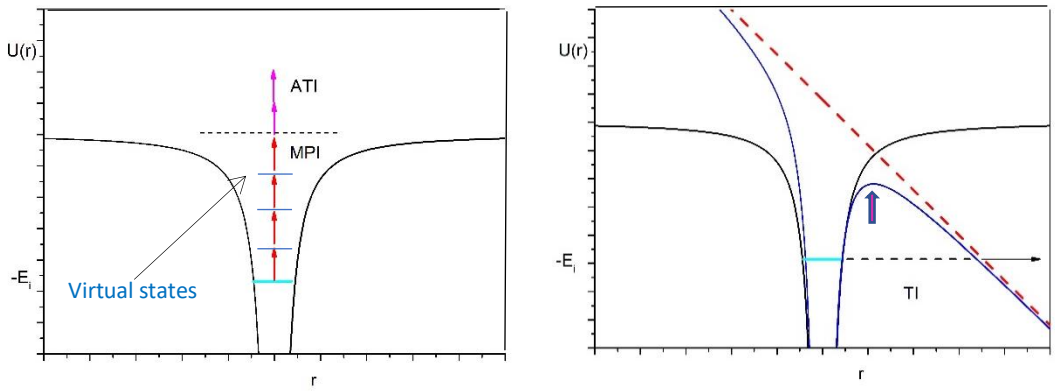

Figure 1: *Graphic representation of the multiphoton (left panel) and tunnel ionization (right panel). The red arrows in the left panel indicate multiple photons absorbed (see text for more detailes). The black curves on the right panel indicate the Coulomb potential. The red dashed line the external electric field (during the first half of the laser cycle). The blue line is derived from the superposition of the black and red lines. In the case of OTBI, the peak of the "bent" indicated with the upward arrow falls below E_i.*

(i) ***Multiphoton ionization (MPI)***: The MPI involves a multiphoton transition from a bound state to a free (continuum) state through a series of virtual states (left panel of Figure 1) and requires laser intensities of the order of 10^{13}-10^{14} W/cm^2. In this regime, the binding potential is quite larger than the laser intensity and, thus, the latter can be treated as a perturbation to the binding potential (Frank 2011). The ionization rate for MPI, R_N, can be calculated (Protopapas et al. 1997) from

$$R_N = \sigma_N I^N \quad (1)$$

where N is the minimum number of photons required to ionize the atom, $\sigma_N\ is$ the generalized cross section and I is the intensity of the laser. For even lower values of the laser intensity, the lowest-order perturbation theory (LOPT) is applied to the atomic system.

An interesting effect encountered in MPI is that a larger number of photons may be absorbed than the minimum necessary to cause ionization. This is called "***Above Threshold Ionization***" (ATI) and it is indicated with the magenta colored arrows in the left panel of Fig. 1. The physical cause of ATI lies in the field distortion of the atomic potential attributed to the effect of the field acting on the atom. ATI is a direct consequence of the absorption of photons by the photoionizing electron that leaves the atom while it still experiences the Coulomb force of the atom and is affected by the atomic potential (Protopapas et al. 1997). To derive the ionization rate in this case, higher order terms must be taken into consideration in the laser-matter interaction, resulting in a simple generalization of eq. (1) (Protopapas, et al. 1997, Gontier and Trahin 1980)

$$R_N = \sigma_{N+S} I^{\mathrm{N+S}} \tag{2}$$

where S is the number of additional photons absorbed.

(ii) ***Tunnel ionization (TI):*** For higher laser intensities, the electric field of the laser can bend the binding potential, thus reducing the height of the barrier the electron needs to surpass, as long as the phase of the laser field is appropriate (Frank 2011). As the barrier becomes lower, the electron is more likely to tunnel through to the continuum. This is shown in the right panel of Figure 1: The superposition of the laser field (red dashed line) and the binding potential (black curve) results in the suppression of the barrier (blue curve to the right), in the first half of the laser cycle, i.e. while the electric field is positive. In the second half of the laser field oscillation

cycle, the electric field will change direction, pushing the electron away from the continuum, so the electron would face a higher barrier (in this case the right panel of Fig. 1 would be reversed, with the red dashed line having the opposite inclination). The rate of TI depends on the exact shape of the binding potential and the properties of the driving field (Orfanos 2020).

(iii) ***Over the Barrier ionization (OTBI):*** When the field interacting with the atom is very intense, the potential barrier is suppressed to such a great extent that the potential barrier goes below the ground state of the bound electron. Consequently, the electron is moving freely into the continuum without the necessity to tunnel through the barrier. If the laser intensities surpass the OTBI threshold, the ionization rate is no longer time dependent. In Fig. 1 (right panel) the peak indicated with the arrow would fall below the energy of the ground state $(-E_i)$.

Following the ionization of the atom, the electron is moving into the continuum while the interaction between the laser electromagnetic field and the electron is maintained, leading to an acceleration of the electron (Orfanos 2020). In the Strong-Field Approximation the field of the ion plays at most a perturbative role (in the following it is completely ignored). The cycle averaged kinetic energy that the electron acquires, while being accelerated under the influence of the oscillating laser electric field, can be simply derived by solving the differential equation of motion of the electron under the influence of the Lorentz force $\vec{F} = qE_0 \cos(\omega t)\hat{x}$, acting on it:

$$m\frac{d^2x}{dt^2} = m\frac{dv}{dt} = eE_0\cos(\omega t) \quad (3)$$

from which we get

$$\frac{dx}{dt} = \frac{eE_0}{m\omega}\sin(\omega t) \quad (4)$$

and therefore

$$E_{kin} = \frac{1}{2}mv^2 = = \frac{e^2E_0^2}{2m\omega^2}sin^2(\omega t) \quad (5)$$

where e is the charge and m is the mass of the electron.

The ***ponderomotive energy*** **(or *quiver*, or *jitter* energy)** of the electron is its average kinetic energy over one cycle, and can be written as (using, also, that $I = \frac{c\epsilon_0 E_0^2}{2}$),

$$U_p = < \frac{1}{2}mv^2 > = \frac{e^2E_0^2}{4m\omega^2} = \frac{e^2I}{2c\epsilon_0 m\omega_0^2} = \frac{2e^2}{c\epsilon_0 m}\cdot\frac{I}{4\omega_0^2} \Rightarrow$$

$$U_p(\text{eV}) = 9.33 \times I(10^{14}\text{W/cm}^2) \times \lambda(\mu\text{m})^2 \quad (6)$$

where I is the laser intensity in 10^{14}W/cm^2 and λ is the laser wavelength in μm.

Using the ponderomotive energy and the ionization potential one can calculate the so-called *Keldysh,* or *adiabaticity,* parameter, γ, which can be used to distinguish between the MPI and TI strong-field ionization regimes. It is given by the expression (Long aTnd Liu 2010)

$$\gamma = (\frac{I_p}{2U_P})^{\frac{1}{2}} = \frac{T_{tunnel}}{T_{laser}} \quad (7)$$

where U_p is given by eq. (6), I_p is the ionization potential of the atom, $T_{tunnel} = 2\pi\frac{\sqrt{2mI_\text{p}}}{eE_0}$ (8) is the time needed for the electron to tunnel through the energy barrier and T_{laser} is the oscillation period of the laser field. The quantity γ depends on specific experimental parameters, namely the laser wavelength and intensity. When γ > 1 at a specific ionization potential, the period of the laser oscillation is shorter than the tunneling time. Thus, there is an increased probability that multiple photons will be absorbed (MPI), whilst the probability that electrons will tunnel to the continuum is smaller. If γ < 1, the time essential for the electron to tunnel is small compared to the laser period. Therefore, it is more likely that tunneling (TI) will take place, while multi photon absorption has limited probability.

2.2 High Harmonic Generation (HHG) with linearly polarized driving field

High-order harmonic generation (HHG) is an important non-linear strong-field physics phenomenon, in which coherent high-frequency radiation is emitted, as a result of the interaction of a strong laser pulse with matter (normally, a gas). It was first reported independently by two groups McPherson et al. (1987) and Ferray et al. (1988). The HHG radiation displays a spectrum of integer multiple frequencies of the driving laser frequency (often referred to as a "frequency comb"), with a plateau where the harmonics have about the same intensity over a large range of harmonic frequencies, followed by a steep cut-off. The exact form of the HHG spectrum depends on the specific experimental setup and the properties of the driving field - e.g. focused laser intensity, pulse duration and wavelength, state of polarization, the target material etc. If low laser intensities interact with the

interacting medium, the emitted frequencies are of low order, whereas, for higher intensities higher order frequencies are produced. As it will explained later, because of the inversion symmetry of the atom in the gas phase, the harmonics produced are odd multiples of the fundamental frequency (Lewenstein et al. 1994).

2.2.1 Single Atom Response-The Three Step Model

The so-called **three step model**, introduced in the early 1990's by Corkum (1993), Kulander et al. (1993), is a semiclassical approach providing a qualitative description of HHG through three steps: *First*, the electron tunnels through the Coulomb barrier of the atom, which is suppressed by the laser field (see previous section) and finds itself in the continuum with zero initial velocity. This normally occurs when the oscillating laser field reaches its maximum value. Then (*second step*), the electron is accelerated by the laser field, following a classically determined trajectory, which under certain conditions (i.e. when the field phase is suitable) can lead the electron back to the parent ion. The quiver or ponderomotive energy of the electron, acquired from the electronic motion in the laser field, is converted into radiation, when the electron recombines with its parent ion (*third step*). The time t_i at which the electron is ionized, dictates whether the electron will return to the ion, as it determines the phase of the laser field at the time of ionization.

The tunneling probability is quite similar for a wide range of phases of the electric field. Thus, electrons produced at different phases around the peak of the laser field (so, at different t_i), acquire different kinetic energies and recombine with the ionic core at different times t_r, but with similar probabilities, thus generating an approximately constant conversion efficiency to XUV photons over a large spectral range (Skantzakis 2011, Orfanos 2020).

The three-step model predicts that the maximum kinetic energy that an electron can accumulate before returning to the ionic core is:

$$E_{max} = I_p + 3.17U_p \quad (9)$$

When an electron recombines with the parent ion, it transfers energy to the generated photons. The yield for a single atom relies on the quantum mechanical probability of ionization and recombination. Equations (6) and (9) indicate that the cut-off energy is determined by the laser frequency and the field strength (and the atomic species used for the interaction). So, the combination of lower laser intensity with lower laser fundamental frequency can lead to the same cut-off energy as a higher laser intensity combined with higher frequency (shorter wavelength), but in the former case the harmonic generation efficiency would be lower, because the spread of the electronic wavepacket causes a decline of the probability for recombination with the core (e.g. Skantzakis, 2011).

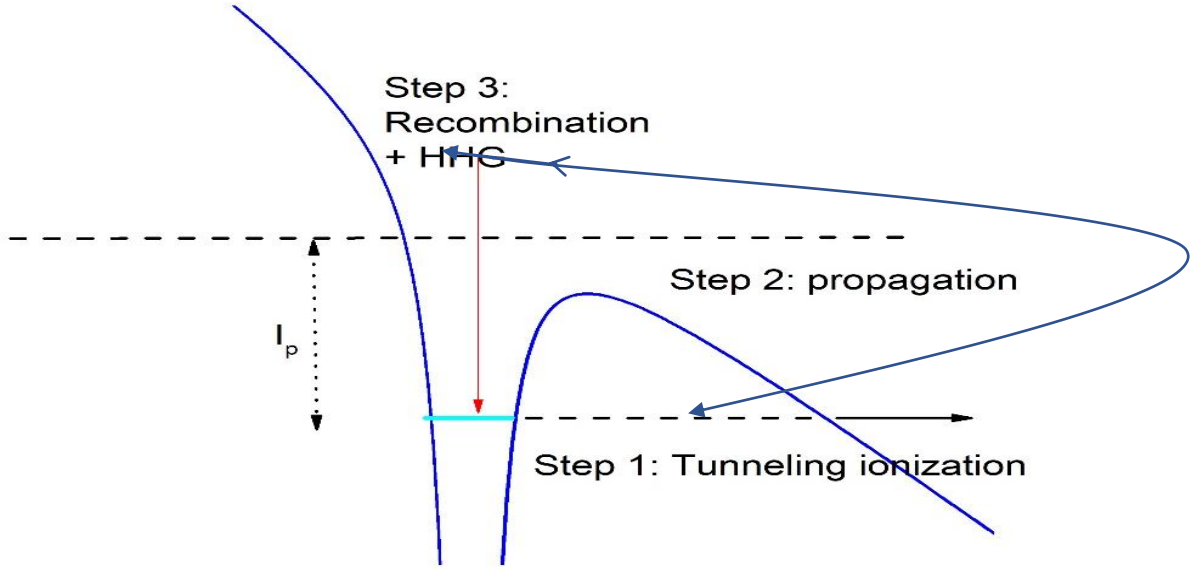

Figure 2. *Graphic representation of the three step model*

2.2.2 Lewenstein Model or Strong Field Approximation for HHG

The strong field approximation (SFA) is a model predominantly used to describe the interaction of an intense laser field with atoms or molecules, and assumes that the dynamics of the electron in the continuum are controlled by the laser field and not by the ion (Lewenstein et al. 1994, Le et al. 2016). The SFA is often considered as the quantum mechanical analog of the three-step model. It uses certain approximations and simplifications that make the SFA much more efficient numerically than a full solution of the time dependent Schrödinger equation (TDSE): (1) the participation of the excited bound states to the harmonic yield is ignored, (2) the influence of the atomic potential on the motion of the continuum electron is assumed to be a small perturbation negligible to first order, and (3) it is assumed that there is no significant depletion of the ground state of the atomic system, which means that we are in the regime of weak ionization. The SFA model can apply to a low-frequency, high intensity limit (U_p>=I_p), and for high harmonics with energies greater than the ionization potential (Skantzakis 2011).

In all the following we have taken $e = m = \hbar = 1$.

The effect of an intense electric field **E**(t) on an atomic system with one active electron (Single Active Electron - SAE approximation) is described by the following Schrodinger equation:

$$i\frac{\partial}{\partial t}|\Psi(\mathbf{r},t)\rangle = \left(-\frac{1}{2}\nabla^2 + V(\mathbf{r}) + \mathbf{r}\cdot\mathbf{E}(t)\right)|\Psi(\mathbf{r},t)\rangle \quad (10)$$

where V(**r**) is the potential due to the ionic core.

The total Hamiltonian can be considered as the sum of $H_0 = -\frac{1}{2}\nabla^2 + V(\mathbf{r})$, which is the field-free Hamiltonian and of the interaction term, $\mathbf{r}\cdot\mathbf{E}(t)$:

$$H(t) = H_0 + \mathbf{r}\cdot\mathbf{E}(t) \quad (11)$$

Ignoring all bound states other than the ground state (as mentioned above), the wavefunction of the tunnel-ionized electron can be written as the superposition of the wavefunction of the

ground state $|g\rangle$ (which satisfies the equation $H_0|g\rangle = -I_p|g\rangle$) and of all possible continuum states, described by the integral $\int d^3kb(\mathbf{k},t)|\mathbf{k}\rangle$ (where $\mathbf{k}$ is the momentum of the outgoing electron, $|\mathbf{k}\rangle$ is the corresponding continuum eigenstate satisfying $H_0|\mathbf{k}\rangle = \frac{k^2}{2}|\mathbf{k}\rangle$, and $\mathrm{b}(\mathbf{k},\mathrm{t})$ is the corresponding amplitude):

$$|\Psi(t)\rangle = e^{iI_p t}\left[|g\rangle + \int d^3kb(\boldsymbol{k},t)|\boldsymbol{k}\rangle\right] \quad (12)$$

In eq. (12) it is assumed that there is no significant depletion of the ground state of the atomic system. If that is not the case the ground state wavefunction is multiplied by a factor a(t).

Calculation of the induced dipole moment at recombination:

The HHG spectrum, produced from the recombination of the electron and the ion, can be calculated from the time-dependent induced dipole moment $\boldsymbol{D}(t)$, with projections along $\boldsymbol{e}_i$ (i=1,2,3) given by

$$D_i(t) = \mathbf{e}_i \cdot \mathbf{D}(t) = \mathbf{e}_i \cdot \langle\Psi(t)|\mathbf{r}|\Psi(t)\rangle \quad (13)$$

We shall consider the transitions between all possible continuum states and the ground state. The induced dipole moment can be written as:

$$\boldsymbol{D}(t) = \int < g|\boldsymbol{r}|\boldsymbol{k} > b(\boldsymbol{k},t)d^3k \quad (14)$$

The total Hamiltonian can be decomposed as :

$$H(t) = H_F(t) + V(\boldsymbol{r}) \quad (15)$$

where $H_F(t)$ is the Hamiltonian of a free electron in the laser field ($\mathbf{E}(\mathbf{t})$), given by

$$H_F(t) = -\frac{1}{2}\nabla^2 + \mathbf{r}\cdot\mathbf{E}(\mathbf{t}) \quad (16)$$

Then, the time evolution operator for $H(t)$, $U(t,t')$, is defined by must be such that :

$|\Psi(t)\rangle = U(t,-\infty)|\Psi(-\infty)\rangle = U(t,-\infty)|g\rangle$

$U_0(t,-\infty)|g\rangle = e^{iI_p t}|g\rangle$

and

$$U(t,t') = U_{\mathrm{F}}(t,t') - i\int_t^t \mathrm{d}t'' U_{\mathrm{F}}(t,t'')VU(t'',t') \quad (17)$$

where $U_{\mathrm{o}}(t,t')$, is the time evolution operator for $H_0 = -\frac{1}{2}\nabla^2 + V(\mathbf{r})$, and $U_{\mathrm{F}}(t,t')$ is the time evolution operator for $H_F(t)$. In the strong field approximation $V(\boldsymbol{r})$ can be considered just as a small perturbation and $U(t,t') \cong U_F(t,t')$

After some manipulation, using the three equations (17) and eq. (15) we can derive the time-dependent dipole moment (in the strong field approximation) :

$$\boldsymbol{D}(t) = -i\int_{-\infty}^{t} e^{-iI_p t}dt' < g|\boldsymbol{r}U(t,t')\,[\mathbf{r}.\boldsymbol{E}(t')]\,e^{iI_p t'}|\boldsymbol{g} > \quad (18)$$

The eigenstates of the Hamiltonian of the free electron moving in the strong laser field (eq. 16) are given by $\left|\chi_{\mathbf{p}}(t)\right\rangle = |\mathbf{p}+\mathbf{A}(t)\rangle \mathrm{e}^{-i\int_{-\infty}^{t}\mathrm{d}t''\frac{1}{2}[\mathbf{p}+\mathbf{A}(t'')]^2}$ where $\mathbf{A}(t)$ is the vector potential of the electric field (of the laser), i.e. $\boldsymbol{E}(t) = -\frac{\partial \boldsymbol{A}}{\partial t}$ and $\boldsymbol{p}$ is the canonical momentum $\boldsymbol{p} = \boldsymbol{k} + \boldsymbol{A}(\boldsymbol{t})$. We can write $U_F(t,t')$ using these eigenstates, as

$$U_F(t,t') = \int \mathrm{d}^3p \left|\chi_{\mathbf{p}}(t)\right\rangle\left\langle\chi_{\mathbf{p}}(t')\right| = \int \mathrm{d}^3p\{|\mathbf{p}+\mathbf{A}(t)\rangle \mathrm{e}^{-i\int_{-\infty}^{t}\mathrm{d}t''\frac{1}{2}[\mathbf{p}+\mathbf{A}(t'')]^2}\langle\mathbf{p}+$$
$$\mathbf{A}(t')|\mathrm{e}^{i\int_{-\infty}^{t'}\mathrm{d}t''\frac{1}{2}[\mathbf{p}+\mathbf{A}(t'')]^2}\} = \int \mathrm{d}^3p\{|\mathbf{p}+\mathbf{A}(t)\rangle\langle\mathbf{p}+\mathbf{A}(t')|e^{-i\int_{t'}^{t}dt''\frac{1}{2}[\boldsymbol{p}+\boldsymbol{A}(t'')]^2}\} \quad (19)$$

Substituting (19) into (18) and assuming $U(t,t') \cong U_F(t,t')$ we get

$$D(t) = -i\int_{-\infty}^{t}\mathrm{d}t'\int \mathrm{d}^3p\,\langle g|\mathbf{r}|\mathbf{p}+\mathbf{A}(t)\rangle\mathbf{E}(t')\cdot\langle\mathbf{p}+$$
$$\mathbf{A}(t')|\mathbf{r}|g\rangle \mathrm{e}^{-i\{\int_{t'}^{t}\mathrm{d}t''\frac{1}{2}[\mathbf{p}+\mathbf{A}(t'')]^2+I_p(t-t')\}} \quad (20)$$

Substituting <**p**|**r**|g>, which is the dipole matrix element for the bound-free transition, with d(**p**) , and by setting $S(\boldsymbol{p},t,t') = \int_{t'}^{t} dt''\frac{1}{2}[\boldsymbol{p}+\boldsymbol{A}(t'')]^2 + I_p(t-t') = \int_{t'}^{t} dt''\{\frac{1}{2}[\boldsymbol{p}+\boldsymbol{A}(t'')]^2 + I_p\}$ we can simplify eq. (20) as follows:

$$D_i(t) = -i\int_{-\infty}^{t} dt'\int d^3\boldsymbol{p}\; d_i^*(\boldsymbol{p}+\boldsymbol{A}(t'))\boldsymbol{E}(t')\cdot d_i(\boldsymbol{p}+\boldsymbol{A}(t))e^{-iS(\boldsymbol{p},t,t')} \quad (21)$$

In the case of hydrogen-like atoms the dipole matrix element for bound-free transitions can be approximated by:

$$d(\boldsymbol{p}) = i(\tfrac{1}{\pi\alpha})\tfrac{3}{4}\tfrac{\boldsymbol{p}}{a}\; e^{-\frac{\boldsymbol{p}^2}{2a}} \quad (22)$$

The integral in equation (19) depicts in a tangible way the physical process of HHG through the quasi-classical three step model: $\boldsymbol{p}$ can be characterized as the classical canonical momentum, because the continuum electron does not sustain the influence of the ionic potential during its motion in the continuum, so the canonical momentum is a conserved quantity; $\boldsymbol{p}+\boldsymbol{A}(\boldsymbol{t})$ can be taken as the instantaneous velocity at time t; the factor $\mathbf{E}(\mathrm{t}')\cdot<\mathbf{p}+\mathbf{A}(\mathrm{t}')|\,\mathbf{r}\,|\mathbf{g}>e^{\mathrm{i}I_p\mathrm{t}'}$ corresponds to the ionization process which takes place at time t' while $e^{-iI\mathrm{p}t}$<g | **r | p + A(t)>** is related to the amplitude of photorecombination at time t. The factor $e^{-i\int_{t'}^{t}\mathrm{d}t'\frac{1}{2}[\boldsymbol{p}+\boldsymbol{A}(t'')]^2}$ is the phase of the electronic wavepacket accumulated from *t'* to *t* while propagating in the continuum.

When the electron returns to the atom and recombines with the ionic core, a photon is emitted as a result of the sum of all induced dipole moments from all ionization times t'<t and all canonical momenta $\boldsymbol{p}$. The factor $S(\boldsymbol{p},t,t')$ in equation (21) is the so-called quasi-classical action. It also entails some effects correlated with the ionization and recombination process through its dependence on I_p (equation 21).

Usually, instead of equation (21), the saddle point approximation is applied, to calculate the integral over the 3D momenta, leading to a simpler form for $S(\boldsymbol{p},t,t')$**.** This approximation is described in the following paragraph.

Application of the saddle-point approximation

Because the term that contains the quasi-classical action and phase of the exponential factor in the integral (21) has a small contribution to the integral as it is a fast oscillating term, the bigger contribution stems from the integrand in the proximity of the saddle points given by the saddle point equation, which, in our case, can be written in a vector form as:

$$\nabla_p S(\boldsymbol{p},t,t') = \nabla_p\int_{t'}^{t}\mathrm{d}t''([\boldsymbol{p}+\boldsymbol{A}(t'')]^2 + I_p) = 0 \;\Rightarrow$$

$$\nabla_p S(\boldsymbol{p},t,t') = \int_{t'}^{t} \nabla_p[\mathbf{p}+\mathbf{A}(\mathbf{t}'')]\cdot[\boldsymbol{p}+\boldsymbol{A}(t'')]\,\mathrm{d}t'' = 0 \Rightarrow$$

$$\nabla_p S(\boldsymbol{p},t,t') = \int_{t'}^{t} [\boldsymbol{p}+\mathbf{A}(t'')]\mathrm{d}t'' = 0 \Rightarrow$$

$$\boldsymbol{p}_s = -\frac{1}{t-t'}\int_{t'}^{t} \mathbf{A}(\mathrm{t}'')\mathrm{d}t'' \tag{23}$$

Since $\nabla_p S(\boldsymbol{p},t,t') = \int_{t'}^{t}\mathbf{v}(\mathrm{t}'')\mathrm{d}\mathrm{t}'' = \boldsymbol{r}(t'')-\boldsymbol{r}(t')$ (24), one can interpret eq. 23 as showing that an electron ionized at time t' returns to the same position at time t, from the trajectory characterized by a canonical momentum $\boldsymbol{p_s}$.

Application of the saddle point approximation to a three-dimensional integral, as is the case here, introduces a term proportional to $(t-t')^{-3/2}$ (see e.g. Le 2016) and the dipole moment is approximated by

$$\begin{aligned}\mathbf{D}(t) = -i\int_{-\infty}^{t}\mathrm{d}t'\left(\frac{-2\pi i}{t-t'-i\epsilon}\right)^{J/2}\mathrm{d}^*(\boldsymbol{p}_s+\mathbf{A}(t))\mathbf{E}(t') \\ \cdot\,\mathrm{d}\big(\boldsymbol{p}_s+\mathbf{A}(t')\big)\mathrm{e}^{-iS(\mathbf{p}_s,t,t')}\end{aligned} \tag{25}$$

with $\boldsymbol{p_s}$ given by eq. 23.

Here ε is an arbitrary small positive number introduced to remove the singularity caused when t is equal to t'. When the saddle point approximation is applied to the integral over $\boldsymbol{p}$, a factor $(t-t')^{3/2}$ appears, which is related to the quantum diffusion effect, i.e. the spread of the wave packet of the continuum electron. As $t-t'$ increases, i.e. when the electron spends more time in the continuum, $\mathbf{D}(t)$ decreases, so the contribution to the harmonic yield is reduced.

Up to this point our discussion is applicable to any laser field. We will now examine two special cases of interest: First, the simplest case of a linearly polarized monochromatic laser beam and second, a bicircular field constructed from two counter-rotating beams of frequencies ω and 2ω.

a. Production of linearly polarized HHG using linearly polarized monochromatic field

By obtaining the Fourier transform of eq. 25 we can derive the HHG power spectrum. For example, if the laser field is linearly polarized, e.g. along the $i=1$ axis, then from eq. 23 it is clear that $\boldsymbol{p_s}$ is also along the same axis and eq. 25 becomes

$$\begin{aligned}\mathrm{D}_1(t) = -i\int_{-\infty}^{t}\mathrm{d}t'\left(\frac{-2\pi i}{t-t'-i\epsilon}\right)^{J/2}\mathrm{d}_1{}^*(p_s+\mathrm{A}(t))\mathrm{E}(t') \\ \cdot\,\mathrm{d}_1\big(p_s+\mathrm{A}(t')\big)\mathrm{e}^{-iS(\mathrm{p}_s,t,t')}\end{aligned} \tag{26}$$

and its Fourier transform gives the HHG power spectrum (which is, clearly, also linearly polarized)

$$P(\omega) \propto \omega^3|D_1(\omega)|^2 \tag{27}$$

where,

$$D_1(\omega) = \int_{-\infty}^{\infty} D_1(t)\mathrm{e}^{i\omega t}\mathrm{d}t = -i\int_{-\infty}^{\infty}\mathrm{d}t\int_{-\infty}^{t}\mathrm{d}t'\left(\frac{-2\pi i}{t-t'-i\epsilon}\right)^{3/2}\mathrm{d}_1{}^*(p_s+\mathrm{A}(t))\mathrm{E}(t')\mathrm{d}_1\big(p_s+\mathrm{A}(t')\big)\mathrm{e}^{-iS((\mathrm{p}_s,t,t')-\omega t} \tag{28}$$

One then needs to apply the saddle point approximation for the double integral (over t and t'), finally leading to the determination of the so-called quantum orbit that the electron follows as it moves in the laser electric field. For a given value of frequency ω, the solutions to the corresponding saddle point equations are a series of saddle points $(p_s, t_{s,} t_{s'})$, that lead to the calculation of the ionization and recombination times for all the electron quantum paths.

Assuming a monochromatic linearly polarized laser field $E(t) = E_0 \cos\left(\frac{2\pi}{T_L} t\right)$ (29), the dipole moment will satisfy the condition $D\left(t + \frac{T_L}{2}\right) = -D(t)$ (30). This condition results in the HHG spectrum containing **only odd harmonics** (see e.g. Le 2016): We define the half cycle dipole moment as $D_{1/2}(t) = -D(t) \ \ for\ -\frac{\pi}{2\omega_L} < t \leqslant \frac{\pi}{2\omega_L}$ and 0 for all other t (31). Using this definition, we can write $D(t) = \sum_{n=-\infty}^{\infty} (-1)^n D_{1/2}\left(t + n\frac{T_L}{2}\right)$ and its Fourier transform as

$$D(\omega) = \sum_{n=-\infty}^{\infty} (-1)^n \int_{-\infty}^{\infty} D_{1/2}\left(t + n\frac{T_L}{2}\right) \mathrm{e}^{i\omega t} \mathrm{d}t \underset{(31)}{\Longrightarrow} D(\omega) =$$

$$D_{1/2}(\omega)\left[\sum_{n=-\infty}^{\infty} (-1)^n \mathrm{e}^{-i\omega n\frac{T_L}{2}}\right] = D_{1/2}(\omega)\left[\sum_{n=-\infty}^{\infty} \mathrm{e}^{i\pi n} \mathrm{e}^{-i\omega n\frac{\pi}{\omega_L}}\right] =$$

$$D_{1/2}(\omega)\left[\sum_{n=-\infty}^{\infty} e^{-i\frac{2\pi n}{\omega_L}\left(\frac{\omega}{2}-\frac{\omega_L}{2}\right)}\right] = D_{1/2}(\omega)\left[\sum_{k=-\infty}^{\infty} \omega_L \delta\left(\frac{1}{2}\{\omega - (2k+1)\omega_L\}\right)\right] =$$

$$D_{1/2}(\omega)[\sum_{k=-\infty}^{\infty} 2\omega_L \delta(\omega - (2k+1)\omega_L)] \Rightarrow$$

$$D(\omega) = \sum_{q\ odd=-\infty}^{\infty} 2\omega_L \delta(\omega - q\omega_L) D_{1/2}(q\omega_L) \qquad (32)$$

It can also be proven (both with the semi-classical approach and with the quantum orbit approach) that each harmonic energy is a result of a **short and a long trajectory**. The first group of quantum paths, labeled as “short trajectories” have electron return times close to one-half of the optical period, while the second group known as “long trajectories” have return times close to one period. The major contribution to the harmonic emission stems from trajectories with return times lower than one optical period. It should be pointed out that the long trajectories generate harmonics with higher yield in comparison with the short trajectories that generate harmonics with lower yield: the electrons that follow the long quantum paths are ionized at the maximum of the electric field pulse, while the short trajectories are followed by electrons ionized at lower electric field strengths and thus with a lower probability.

It is also worth commenting that the Three Step Model and the Saddle Point Approximation have a difference in the cut-off energy, which is slightly higher in the case of the Lewenstein model compared to the semiclassical three step model (given by equation 9) . This happens because the electron is not actually ionized at the ionic core, but at the tunnel exit. Thus, because of the finite spatial difference between the nucleus and the tunneling position, the electron needs to cover some further distance, thus gaining additional kinetic energy as it is accelerated by the laser field and, therefore, the cut-off energy is shifted to the right.

b*. *Production of circularly polarized HHG using two-color co-planar field mixing

As discussed above linearly polarized driving fields (widely used) produce linearly polarized harmonics. Miloševič et al. (2000) proposed an efficient way for the generation of circularly polarized high-order harmonics by using a bi-chromatic laser field composed of two electric fields with frequencies ω and 2ω respectively, which are polarized in the same plane, but their vectors rotate in opposite directions (see also Weber et al. 2021).

Actually, selection rules, which are discussed in Appendix A, allow for $3m+1$ and $3m-1$ harmonics with the sign of their helicity changing from one harmonic to the next. In this counter-rotating scheme originally proposed in Eichmann et al. (1995) the intensity of the circularly polarized harmonics has been estimated to be quite high. In general, counter-rotating circular polarizations yield the highest intensity, compared to other different techniques that produce circular harmonics, within a specific range, excluding too high harmonics. Some of the questions raised concerning the above scheme are the explanation of the substantial intensity of the produced harmonics as well as the nature of the cut-off law.

The driving laser field composed of two elliptically polarized electric fields of frequencies ω and 2ω can be written as:

$$\boldsymbol{E}(\mathrm{t}) = \frac{1}{2i}\left[\frac{E_1}{\sqrt{1+\varepsilon_1^2}}(\boldsymbol{e_1} - \mathrm{i}\varepsilon_1\boldsymbol{e_2})\mathrm{e}^{\mathrm{i}\omega\mathrm{t}} + \frac{E_2}{\sqrt{1+\varepsilon_2^2}}(\boldsymbol{e_1} - \mathrm{i}\varepsilon_2\boldsymbol{e_2})\mathrm{e}^{2\mathrm{i}\omega\mathrm{t}}\right] \tag{33}$$

where E_1 and E_2 are the electric field intensities for each of the two components of the bicircular field, and $\varepsilon_1, \varepsilon_2$ $(-1 \leq \varepsilon_{1,2} \leq 1)$ are the corresponding ellipticities. In most cases, two co-rotating or two counter-rotating circularly polarized fields are characterized by $\varepsilon_1 = \varepsilon_2 = 1$, or, $\varepsilon_1 = 1\ and\ \varepsilon_2 = -1$, respectively. The field described in eq. (33) obeys a particular dynamical symmetry, namely it is unchanged under a simultaneous rotation by 120° and translation by 1/3 of the optical cycle, T/3 (Milošević 2015)

Eq. (33) is used together with eq. (25) to derive the induced dipole moment. In the case of interest here (bi-circular field) the ground state is a p state with magnetic quantum numbers 0,±1. This is the main difference from the result of the previous paragraph, where the dipole matrix elements were calculated for only one wavefunction describing the ground state. Here, we need to sum over the three different matrix elements, corresponding to the wavefunctions with the different magnetic quantum numbers. If we neglect spin, then in a np^6configurationthere are three (instead of 6) active electrons i.e. instead of d(**p**) in eq. (21) onwards, we use $\sum_{a=1,2,3} \mathbf{d}^{(a)}(\boldsymbol{p})_{|_{m_i=m_f=m}} = \sum_m \mathbf{d}_m(t)$, (34) where α=1,2,3 denotes the active electrons and $m = 0, \pm 1$. The dipole matrix elements are calculated by describing the initial state with $\psi_{\alpha i}(\mathbf{r}_\alpha) = Y_{lm_i}(\hat{\mathbf{r}}_\alpha)$ (35), and the final one with $\psi_{\alpha f}(\mathbf{r}_\alpha) = Y_{lm_f}(\hat{\mathbf{r}}_\alpha)$ (36).

It is noted that the cut-off law is not the same as that for linearly polarized harmonics given by eq. (9)**.** If the intensities of the laser fields that compose the total bicircular field are equal, the following cut-off law is derived (Milošević et al. 2000):

$$\mathrm{E}_{max} = 1.2I_\mathrm{p} + (1/\sqrt{2})3.17U_p \tag{37}$$

Qualitatively, we can envisage the generation of the harmonics in the following way. For every harmonic order both the x- and the y-component of the electron's velocity start to increase

under the effect of the laser field. The x-component of the electron's velocity starts to decrease when the x component electric field changes its sign, while the y-component of the electron's velocity starts to increase till the final time t_f, a time point at which both v_y and $|v_x|$ have maxima. During the electron's travel in the continuum, the x- electric field changes its sign from its negative maximum to its positive maximum. Nonetheless, the y-component is initially small and remains small throughout electron's travel. This physical parameter does not affect the return of the electron to the ionic core though, because the y-component of the electron at the beginning is substantial. The initial velocity of the electron that generates each of the harmonics increases as the harmonic order increases. Thus, this increase in the initial electronic velocity explains the lowering of the harmonic yield. This picture of the generation of harmonics repeats itself three times during each periodic oscillation of the electric field, which rotates itself every T/3 by 120^o (see fig. 5 in the next section). The polarization of the harmonics for every T/3 of the laser field oscillation is theoretically largely linear and that could be observed if someone separated the contribution of the laser oscillation for every T/3. Thus, the superposition of the contribution of the dipole moment from each cycle leads to the generation of circularly polarized harmonics.

3. Experimental results

3.1 General description of experimental setup

The experiments were conducted in the “Attosecond Science and Technology” laboratory at the Institute for Electronic Structure and Lasers (at FORTH), using the MW line driven by the Ti-Sapphire pulsed laser, with carrier wavelength of 800nm, pulse duration of 25fs and energy up to 400mJ per pulse.

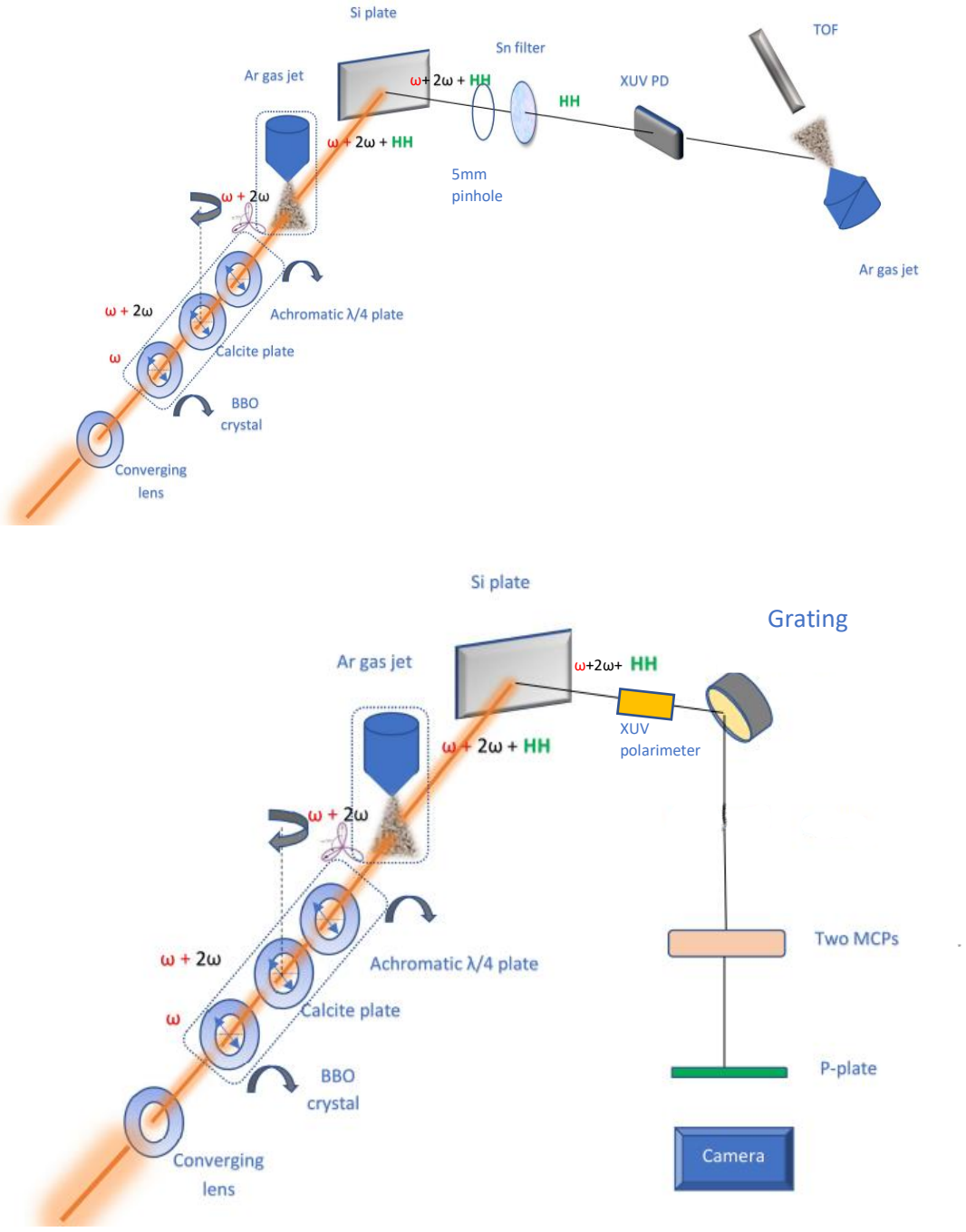

Figure 3. *Schematic representation of the experimental setup.* ***Top panel****: The setup for the spectroscopic characterization of the HHG.* ***Bottom panel****. The setup for the meas''rement of the polarization state of the HHG.*

Figure 3 shows a schematic representation of the experimental setup, which is designed to be operated under vacuum conditions.

The top panel of Fig. 3 depicts the main components of the experimental setup used for the high harmonic generation and its spectroscopic characterization. The experimental setup consists of three different chambers that follow a converging lens of focal length $f = 3m$, that focuses the laser beam, which has an outer diameter of 3cm and energy of up to 32mJ per pulse.

The **first chamber** contains a MAZEL-TOV (MAch-ZEhnder-Less for Threefold Optical Virgina spiderwort) apparatus of 15cm in length, located at a distance of 1.25m from the converging lens. The MAZEL-TOV device (see e.g. Kfir et al. 2016) consists of a Beta-phase Barium Borate Type I (BBO) crystal, a calcite plate and a super achromatic λ/4 phase plate. In this chamber, the "driving field" is produced, as a result from the superposition of two co-planar circularly polarized fields with frequencies ω and 2ω, with opposite helicity.

The **second chamber** is where the high order harmonics are generated (HHG: higher harmonic generation). A pulsed nozzle controls the Ar gas flux in the chamber. Following the HHG chamber, there is a silicon plate inclined at 75° for the redirection of the emerging beam to the third chamber. Following the Si plate, there are two apertures of 5mm diameter. On the second aperture, a thin Sn filter (of 150nm thickness) is attached.

The **third chamber** is where the produced higher harmonics are detected and recorded. It includes an XUV photodiode (XUV PD) for the measurement of the energy of the pulse, a pulsed nozzle that controls the Ar gas flux into the chamber and finally a time-of-flight (TOF) spectrometer, protected by a μ-metal, where the produced radiation is spectrally characterized.

The bottom panel of Fig. 3 concerns the second part of the experiment, where the polarization state of the HHG was measured. The first section of the experimental setup, where the high harmonics are generated, is identical to what was described above. Following the HHG production, there is a system of mirrors that act as a **reflective polarimeter**, followed by a grating that analyzes the HHG spectra, two MCPs, a phosphorus plate and a camera.

3.2 Detailed description of the main components of the experimental setup

3.2.1 The BBO crystal

A Beta Barium Borate (β-BaB2O4) –BBO– is a non-linear, negative, uniaxial and anisotropic crystal that belongs to the point group 3m-C_{3v} (non centro-symmetric). The main "strengths" of a BBO crystal are its wide transmission/transparency range and its broad phase-matching range, which render it ideal for HHG using Nd:YAG and Nd:YLF lasers[1].

In an anisotropic crystal, the phase velocity depends on the polarization state of the light and on the direction of propagation. Generally, in a crystal, the diffraction index values are different in the directions x, y, z. For a uniaxial crystal $n_x=n_y=n_0$ (ordinary index of refraction) and $n_e=n_z$ (extraordinary index of refraction). When $n_0 > n_e$, the crystal is a **negative uniaxial crystal**.

[1] https://www.advatech-uk.co.uk/nlo_bbo.html

Let us consider the response (material polarization, P_i) of a material to an applied electric field (the incident laser field in this case): $P_i = \epsilon_0 X_{ij} E_j + 2d_{ijk} E_j E_k + 4X_{ijkl} E_j E_k E_l + \cdots$. For low intensities, only the linear term is significant. Also, when we have a centro-symmetric crystal, the second order non-linearity is zero (regardless of the intensity). In a non centro-symmetric crystal, in the high intensity regime, $d_{ijk} \neq 0$ and P_i will have a component with twice the incident optical frequency:

$$P_i(t) = 2d_{ijk} E_j(t) E_k(t) = 2d_{ijk} \frac{\left(\tilde{E}_j e^{i\omega_1 t} + \tilde{E}_j^* e^{-i\omega_1 t}\right)}{2} \frac{\left(\tilde{E}_k e^{i\omega_2 t} + \tilde{E}_k^* e^{-i\omega_2 t}\right)}{2} =$$
$$\frac{1}{2} d_{ijk}\left(\tilde{E}_j \tilde{E}_k^* e^{i(\omega_1 - \omega_2)t} + \tilde{E}_j^* \tilde{E}_k e^{-i(\omega_1 - \omega_2)t} + \tilde{E}_j \tilde{E}_k e^{i(\omega_1 + \omega_2)t} + \tilde{E}_j^* \tilde{E}_k^* e^{-i(\omega_1 + \omega_2)t}\right),$$

where $\tilde{E}_j = E_j(\omega_1, z) e^{-ik_1 z}$ and $\tilde{E}_k = E_k(\omega_1, z) e^{-ik_1 z}$

If $\omega_1 = \omega_2 = \omega$, then $P_i(t) = \frac{1}{2} d_{ijk}\left(\tilde{E}_j \tilde{E}_k e^{i2\omega t} + \tilde{E}_j^* \tilde{E}_k^* e^{-i2\omega t}\right)$, i.e. the polarization has twice the frequency of each field. This discussion briefly describes the second harmonic generation in a non centro-symmetric non-linear crystal. Now we shall discuss what happens to the ω and 2ω fields as they propagate in the BBO crystal.

In an anisotropic crystal such as the BBO, the index of refraction for the extraordinary beam depends on the direction of propagation with respect to the axis of the crystal, so away from the optical axis, there is a non-negative birefringence $\Delta n = n_o - n_e$, which depends on the angle and on λ (and weakly on temperature).

Using again $P_i(t) = 2d_{ijk} E_j(t) E_k(t)$ but for the ω and 2ω fields, we get, after some manipulation, for the resulting non-linear polarization $P_{NL}(\omega, z, t) = 2d_{eff} E_3(2\omega, t) E_1^*(\omega, t) e^{i(k_{2\omega} - 2k_\omega)z}$. In order to have the fundamental and second harmonic polarization in phase, we need to have $k_{2\omega} - 2k_\omega = 2k_\omega - k_{2\omega} = 0 \Rightarrow 2k_\omega = k_{2\omega}$ $\Rightarrow 2[\omega\sqrt{\varepsilon\mu} n_\omega] = (2\omega)\sqrt{\varepsilon\mu} n_{2\omega} \Rightarrow n_\omega = n_{2\omega}$. This is the phase matching condition needed to achieve efficient generation of the second harmonic. This condition can be achieved at a specific angle θ in the crystal. In negative crystals (such as BBO) two ordinary waves with the same direction of polarization can generate an extraordinary second harmonic wave. This is called **type I phase matching** and is symbolized by o + o → e (Popmintchev et al. 2009)[2]. So, for this type of phase matching, $2k_{o\omega} = k_{o\omega} + k_{o\omega} = k_{c(2\omega)}(\theta)$ and $n_{o(\omega)} = n_{e(2\omega)}(\theta_m)$, where θ_m is the phase matching angle. In our case $\lambda_\omega = 800nm$ and $\lambda_{2\omega} = 400nm$. Applying the known relation for birefringent crystals, $\frac{1}{n_{e(\omega)}^2(\theta)} = \frac{\cos^2(\theta)}{n_{o(\omega)}^2} + \frac{\sin^2(\theta)}{n_{e(\omega)}^2}$ (e.g. Woehlecke et al., 2005), we find that $\sin^2(\theta_m) = \frac{n_{o(\omega)}^{-2} - n_{o(2\omega)}^{-2}}{n_{e(2\omega)}^{-2} - n_{o(2\omega)}^{-2}}$.

Given that for BBO $n_0^2 = 2.7359 + 0.01878/(\lambda^2 - 0.01822) - 0.01354\lambda^2$ and $n_e^2 = 2.3753 + 0.01224/(\lambda^2 - 0.01667) - 0.01516\lambda^2$ ([3]), where λ in μm, we can calculate θ_m *to be* $\sim 29.2^o$ (see also [4]).

[2] It is noted that type II phase matching is also possible, but at an angle of ~42°

[3] https://www.unitedcrystals.com/BBOProp.html

[4] https://www.pmoptics.com/beta_barium_borate.html

The BBO crystal used here has a thickness of 0.2mm and is cut at an angle of 29.20°, which, as we saw, is the appropriate angle for SHG (second harmonic generation) Type I (oo→e) phase-matching for $\lambda_{fundamental} = 800nm$.

3.2.2 TOF Spectrometer

The beam enters the TOF spectrometer, where the spectral characterization of the XUV radiation takes place. This is achieved by measuring the energies of the photoelectrons produced by the interaction between the incident unfocused XUV radiation and the Ar atoms which are injected in the chamber through a nozzle. The Ar atoms become ionized. The photoelectrons produced have kinetic energies $E_{kin} = hv_{XUV} - I_P$, where $I_P = 15.759eV$ is the ionization energy of Ar. Due to the different velocities of these photoelectrons, $\upsilon = \sqrt{\frac{2E_{kin}}{m}}$, the time of their travel in the TOF tube of length L, given by $t_{flight} = L/\upsilon = L/\sqrt{\frac{2E_{kin}}{m}} = \sqrt{\frac{mL^2}{2E_{kin}}} = \sqrt{\frac{mL^2}{2(hv_{XUV} - I_{P)}}}$, depends on the incident XUV photon energy hv_{XUV}. Thus, one can derive the spectrum of the incident XUV radiation from the distribution of the TOF (t_{flight}) of the photoelectrons (Vassakis et al. 2021), as detected by a pair of Micro-channel plates.

3.2.3 MCP – microchannel plate

The microchannel plate (MCP) is a specially fabricated plate that amplifies an electron signal, similar to a secondary electron multiplier. The MCP consists of a two-dimensional periodic array of several million independent channels each working as an independent electron multiplier. When an electron (or ion, or photon) enters one of these channels, it hits the inner wall of the channel, which is covered with a semi-conducting material, causing the emission of a secondary electron, which is accelerated by an applied electric field and, following a parabolic path, it hits the wall again thus producing another secondary electron. This process is repeated many times along the channel, thus resulting in an avalanche of several thousand to a million electrons, emerging from the channel[5]. As the produced charge is highly localized in each one of the millions of channels, the MCP can be used as a high spatial resolution photon and particle imager. In addition, due to the small length of each individual electron multiplier (each channel), the timing of the photon/particle impact can be determined very accurately (to better than 100 psec), thus yielding high temporal resolution. It is the latter property, along with the high gain, that renders MCP detectors uniquely suited for TOF spectroscopy.

In the present experiment, the photoelectrons produced by the ionization of Ar atoms fall onto the first MCP, where they are multiplied, and then pass through a second MCP before reaching the anode, where the arrival time of the signal is recorded. When only a single MCP stage is used there are saturation effects in the pore, so for ultra-low light-level two or more MCP are stacked in series. A single MCP stage shows saturation effects in the pore so that for ultra-low flux-level two or more MCP are stacked in series. [6]

[5] http://www0.mi.infn.it/~sleoni/TEACHING/Nuc-Phys-Det/PDF/papers/MCPbrochure.pdf
[6] https://www.atom.uni-frankfurt.de/research/10_COLTRIMS/20_MCP-detectors/

3.2.4 The polarimeter and spectrograph

The polarimeter, used for the second experiment, contains three mirrors (Ag, Al, Ag) placed at certain positions, forming specific angles with respect to an axis perpendicular to the mirror. The values of the angles are 75°, 60°,75° for each one of the mirrors. Following the polarimeter, there is a grating spectrometer that analyses the HHG beam into its spectral components. The experimental setup also contains two MCPs that generate the photoelectrons that subsequently fall upon the phosphorus screen to produce the photons that are then detected by a CCD camera (Figure 3).

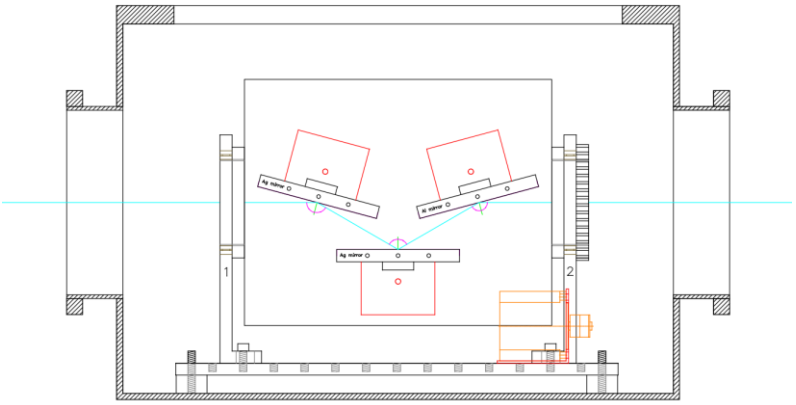

Figure 4. Design of the XUV polarimeter. The three mirrors are placed at different angles. The polarimeter was constructed as part of E. Vassakis PhD thesis.

3.2.5 Detailed description of the experimental process for the first experiment

The initial laser beam passes through a converging lens of 3m focal length. The incident laser beam is p-polarized. As it passes through the BBO, about 30% of the energy of the initial pulse, is transformed to the second harmonic field, which is s-polarized. The second harmonic has half the wavelength of the incident beam, corresponding to 401nm. Both the ω and 2ω beams are focused at the same location along the propagation axis, in the Ar chamber.

Following the BBO, the beam of the two linearly (perpendicular to each other) polarized fields (with frequencies ω and 2ω) passes through a calcite plate (with almost normal incidence) in order to compensate for group velocity delays between the ω and 2ω fields, caused by the BBO, as well as to *pre*-compensate for delays introduced by the retardation plate that follows. This ensures that the ω and 2ω beams will reach the focus (in the 2nd chamber where the Ar nozzle is) with negligible differences in the group velocity. The calcite plate has anti-reflection coating and a group velocity delay compensation range 310-450 fs.

Subsequently, the beam, goes through the super achromatic quarter wavelength retardation plate (QWP). This results in two counter-rotating circularly polarized fields[7] with frequencies ω, 2ω. If the partial intensities of the ω and 2ω fields, I_{ω} and $I_{2\omega}$, are approximately equal, then the electric field vector of the resulting bicircular field is described by the shape shown in Figure 5.

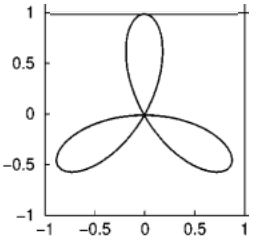

Figure 5. *The electric field of the ω-2ω counter-rotating circularly polarized laser field plotted for a whole period T=2π/ω, for equal partial intensities (from Milosevic et al. 2000).*

These co-propagating bichromatic laser beams (the fundamental and second harmonic) that are circularly polarized with opposite helicities, constitute the driving fields for the high harmonic generation (HHG) that takes place in the second chamber. Assuming that the beams (ω and 2ω) are Gaussian, it is estimated that the two components of the bicircular field have intensities $I_{\omega} \approx I_{2\omega} \approx 1x10^{14} W/cm^2$ at the focus. As the bicircular field passes through the Ar jet (whose flux is controlled by the nozzle), located at the focus, high order harmonics are generated (as explained in Section 2). These harmonics have frequencies in the extreme ultraviolet (XUV). The produced XUV radiation propagates together with the bicircular field towards a Si plate at an angle of incidence of 75°. Reflection on the plate, redirects the beam towards the third chamber, while at the same time it reduces significantly the p-component of the co-propagating bicircular field. This is due to the fact that the reflectivity of the Si plate for p-polarized light is very low at 75° (and even lower for λ=800nm compared to shorter wavelengths). On the other hand, the XUV beam is reflected by ~60%. Between the Si plate and the third chamber there are two apertures that cut out the outer wings of the remaining bicircular beam, while allowing the entire XUV to pass through. In the second aperture there is a Sn filter attached, which removes all of the remaining bicircular field, thus spectroscopically selecting the XUV HHG field (with energies roughly between 17 and 23eV). After the Sn filter, the XUV beam is directed to a calibrated XUV photodiode, to measure the energy of the pulse. Subsequently it enters the detection chamber, where the unfocused incident XUV radiation interacts with the Ar atoms which are injected into the chamber through a pulsed nozzle of controlled flux. For the photon energies of the XUV HHG that are higher than the ionization potential of Ar, atoms become ionized and photoelectrons of different kinetic energies are produced. Each photoelectron travels in the TOF spectrometer different times, depending on its kinetic energy (see Section 3.2.2) and then falls on the pair of the MCPs where it is multiplied and then recorded at the anode. From the arrival time recorded, the energy is determined, and thus the spectroscopic characterization of the XUV HHG radiation is achieved.

[7] If the p- and s-polarized are represented by the Jones vectors $\frac{1}{\sqrt{2}}\begin{pmatrix}1\\1\end{pmatrix}$ and $\frac{1}{\sqrt{2}}\begin{pmatrix}-1\\1\end{pmatrix}$, and the QWP at 45° with the Jones matrix $\begin{pmatrix}1 & 0\\0 & i\end{pmatrix}$ then the emerging field will be left-circularly polarized in the first case, and right-circularly polarized in the second case: $\frac{1}{\sqrt{2}}\begin{pmatrix}1 & 0\\0 & i\end{pmatrix}\begin{pmatrix}1\\1\end{pmatrix} = \frac{1}{\sqrt{2}}\begin{pmatrix}1\\i\end{pmatrix}, LCP$ and $\frac{1}{\sqrt{2}}\begin{pmatrix}1 & 0\\0 & i\end{pmatrix}\begin{pmatrix}-1\\1\end{pmatrix} = -\frac{1}{\sqrt{2}}\begin{pmatrix}1\\-i\end{pmatrix}, RCP$

In the second part of the experiment, the HHG beam, after reflection by the Si plate follows a different path suffering additional reflections which essentially play the role of a polarizer and finally go through the grating, the detection system (MCPs, phosphorous screen recorded with a CCD camera).

3.3 Log of the conducted experiments

The experiment was repeated three times. Two runs were conducted on 25/10/2021 and a third run on 26/10/2021. In every repetition of the experiment, the HHG spectrum was produced for a series of different rotation angles of the BBO. For each different angle, different phase-matching is achieved in the crystal. Thus, for a non-monochromatic pulse with a frequency width of $\Delta\omega$, different frequencies become phase-matched with the incident field. Therefore, for different rotation angles, the wavelength of the produced second harmonic is different. For the seven different angles used, the corresponding central wavelengths of the second harmonic produced had the values 399.00, 399.57, 400.14, 400.71, 401.29, 401.86, 402.43nm. The polarimetric experiment was conducted on 26/03/2022. We obtained measurements of intensity versus polarization angle for the linearly and circularly polarized harmonics.

4. Analysis of results

4.1 First experiment - spectroscopic characterization of the HHG

For each different rotation angle of the BBO, the corresponding spectrum of the produced circularly polarized HHG XUV radiation was recorded using the TOF spectrometer. The data analysis and calibration was performed using a simple Python code (see Appendix C).

The spectra, in their original form, are given as intensity (in arbitrary units) as a function of the recorded time of arrival, t. An example of such a spectrum is provided in Figure 6a. The zero point of each spectrum is determined with respect to the photopeak, which corresponds to the first photons recorded. So, for each spectrum, we determined the location of this peak, t_o, and subtracted this value from all time measurements, yielding a shifted spectrum (intensity as a function of t-t_o), similar to the one shown in Figure 6b.

The next step involved a change of variable, from t-t_o to $1/(t\text{-}t_o)^2$, which is related linearly to the photoelectron kinetic energy (see section 3.2.2):

$$t_{flight} = \sqrt{\frac{mL^2}{2(h\nu_{XUV} - I_P)}} \Rightarrow h\nu_{XUV} = \frac{mL^2}{2t_{flight}{}^2} + I_P \text{ , where } t_{flight} = t - t_o \text{ .}$$

An example of the corresponding spectrum is given in Figure 6c.

Figures 6a,b,and c correspond to a wavelength of 399.00nm for the 2nd harmonic (determined from the BBO rotation angle).

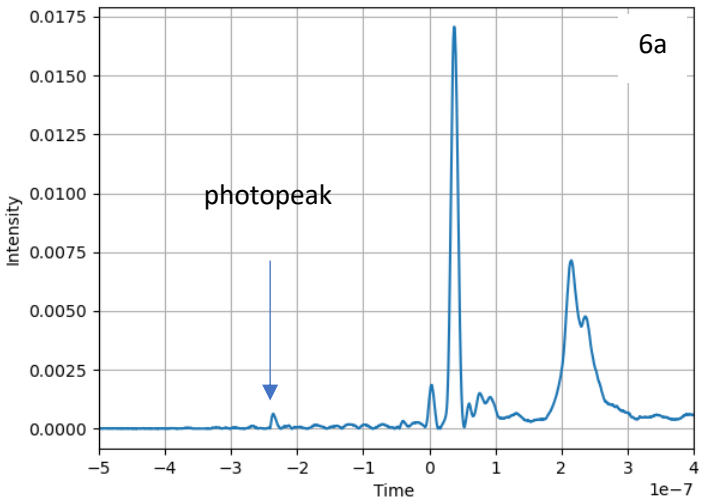

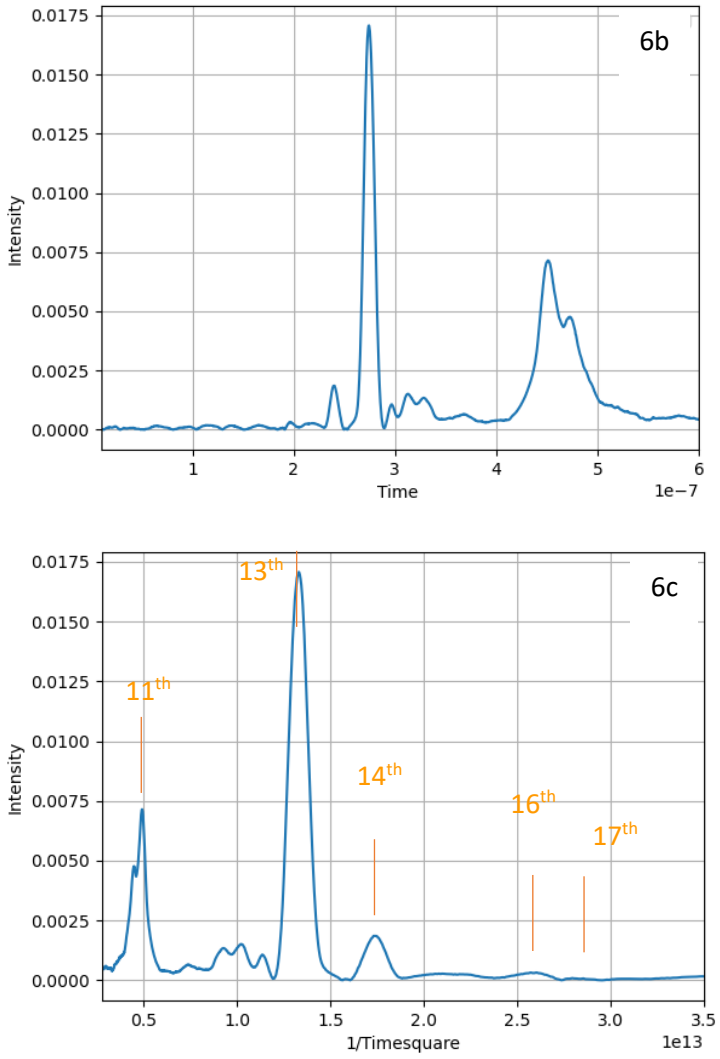

Figure 6*: a. The original spectrum: Intensity (in arbitrary units) as a function of time of arrival (26/10/2021 run, for $\lambda_{2\omega}$=399nm). b. The same spectrum, shifted so that t=0 coincides with the time of arrival of the first photons. c. Intensity as a function of $1/t^2$, which is linearly correlated to the kinetic energy of the photoelectrons, and hence of the corresponding photons. In Orange we mark the location of the different harmonics present in this spectrum.*

This spectrum (for the first value of the rotation angle) is used to calibrate all the spectra obtained during the same run (i.e. at different BBO angles). This is done by recognizing the different harmonics on the spectrum (marked in orange in Fig. 6c) and assigning the appropriate energy (in eV) to the corresponding value of $\frac{1}{t_{flight}{}^2}$ at the center of the peak. The harmonics recognized in the spectra are the 11th, 13th, 14th, 16th and 17th. Their energies are given by $E_m = m \times 1.55\ (eV)$, where m is the order of the harmonic.

Figure 7 shows an example of the calibration relation, which is linear, as expected. The slope of the line should be equal to $mL^2/2 = 0.511MeV \times L^2/2$ (as is indeed the case, assuming $L = 36$cm). The intercept should correspond to the ionization potential of Ar, I_p, which is also the case, within 3% of the bibliographic value.

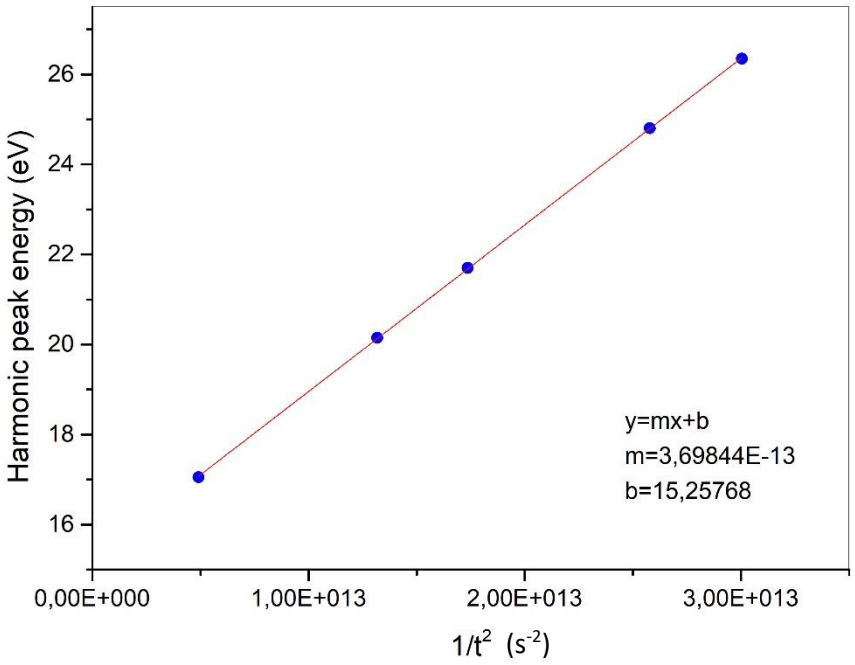

Figure 7*: Example of the calibration curve for the spectrum corresponding to $\lambda_{2\omega}$=399nm, for the 26/10 run.*

The calibrated spectrum of Fig. 6c, which is derived using the calibration curve of Fig. 7, is shown in Figure 8.

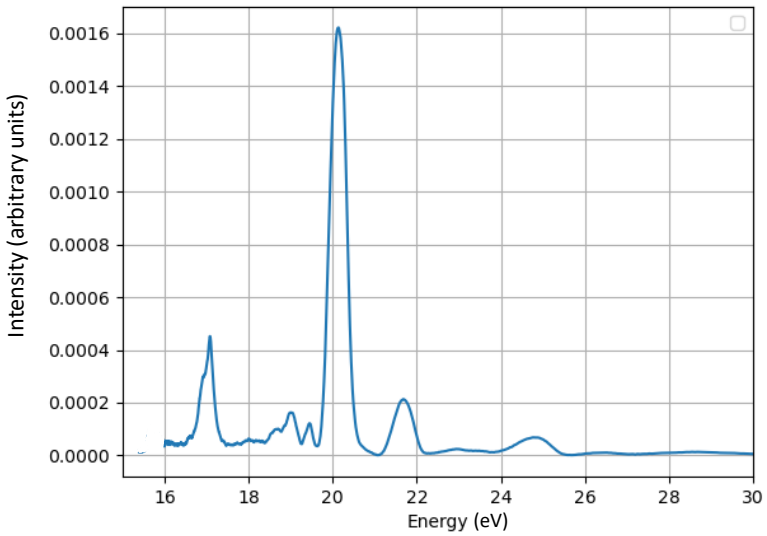

Figure 8*: The spectrum of Fig. 3 calibrated in energy.*

As already mentioned, the calibration derived for $\lambda_{2\omega}$*=399nm* is applied to all spectra of the same run. Figure 9 shows all 7 spectra for the different wavelengths $\lambda_{2\omega}$ of the driving field (for

the run of 26/10). The calibrated spectra were saved as ascii files and further analyzed using Origin 9.4.

It is evident in Fig. 9 that the peaks corresponding to the different harmonics are displaced toward lower energies, as the wavelength of the driver radiation increases. This displacement has been investigated and quantified for all visible harmonics, 11^{th}, 13^{th}, 14^{th}, 16^{th} and 17^{th}. Each harmonic peak in each spectrum was fitted with a gaussian function (an example is shown in Figure 10 for the 13^{th} harmonic). The position (xc), and the height of the peak were recorded for each harmonic, for each spectrum and each run. Tables 1 to 5 list the energies of the centers of the peaks for the 11^{th}, 13^{th}, 14^{th}, 16^{th} and 17^{th} harmonic respectively, along with the corresponding errors. The last column in each one of these tables gives the mean and standard deviation derived from the different runs.

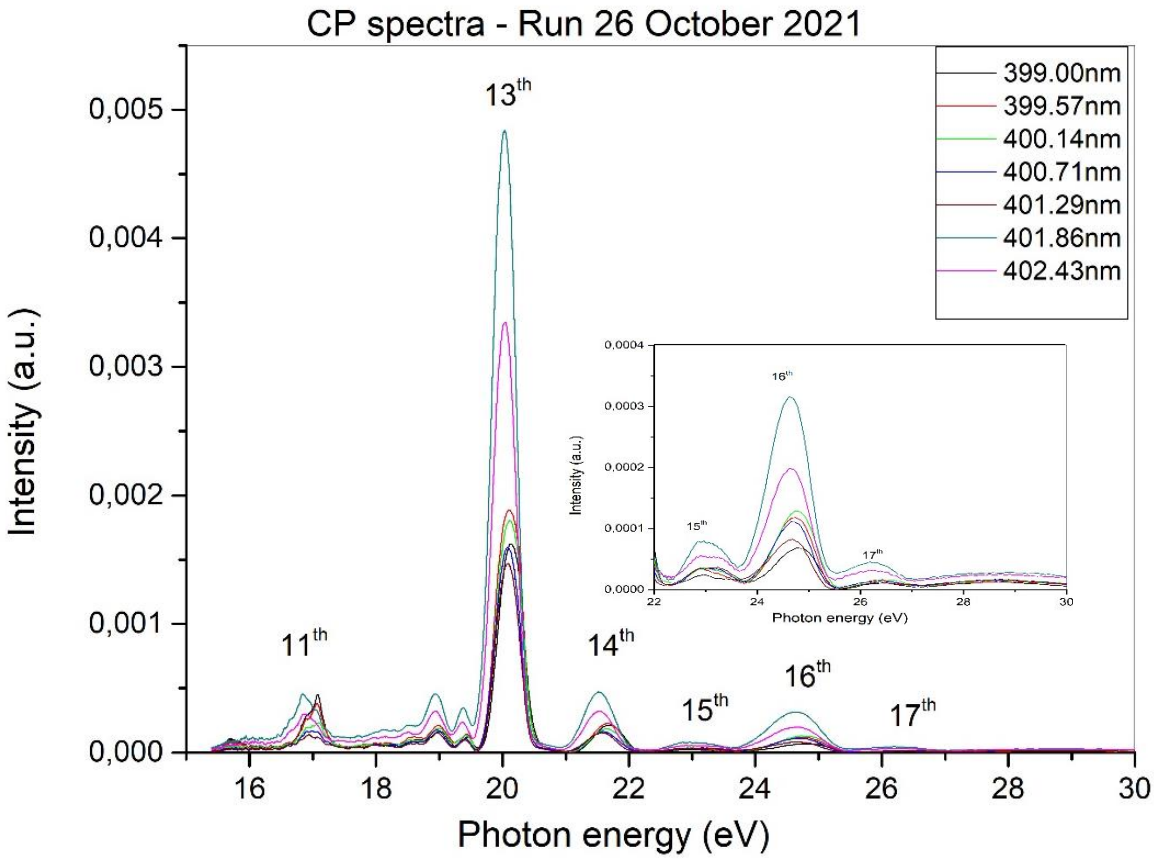

Figure 9: *Calibrated spectra for the circularly polarized harmonics, for seven different values of the driver radiation wavelength, $\lambda_{2\omega}$ (for the 26/10 run).*

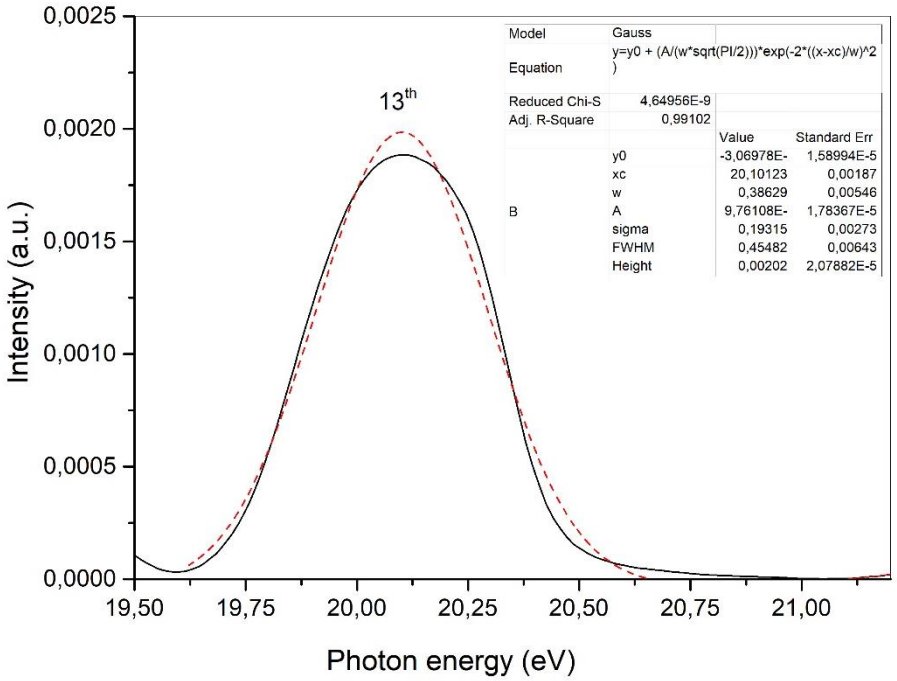

Figure 10: *Example of a gaussian fit to the 13th harmonic peak (for $\lambda_{2\omega}$=399nm) for the 26/10 run.*

Table 1

11th harmonic							
	25/10/2021-run1		**25/10/2021-run2**		**26/10/2021**		
$\lambda_{2\omega}$ (nm)	**E (eV)**	**σE(eV)**	**E (eV)**	**σE(eV)**	**E (eV)**	**σE(eV)**	**<E> (eV)**
399,00	17,02891	0,00172	17,02526	0,00179	17,02475	0,00164	17,026±0,002
399,57	17,02557	0,00129	17,02321	0,00153	17,02346	0,00153	17,024±0,001
400,14	17,02386	0,00125	17,01985	0,00135	17,0201	0,0014	17,021±0,002
400,71	16,9917	0,00118	16,98765	0,00126	16,9878	0,00129	16,989±0,002
401,29	16,9748	0,00136	16,96959	0,00157	16,96959	0,00157	16,971±0,003
401,86	16,89041	8,91914E-4	16,88530	0,00108	16,88534	0,00111	16,887±0,003
402,43	16,9027	9,57724E-4	16,89857	9,697E-4	16,89861	9,75E-4	16,900±0,002

Table 2

13th harmonic							
	25/10/2021-run1		**25/10/2021-run2**		**26/10/2021**		
$\lambda_{2\omega}$ (nm)	**E (eV)**	**σE(eV)**	**E (eV)**	**σE(eV)**	**E (eV)**	**σE(eV)**	**<E> (eV)**
399,00	20,12592	0,00117	20,13024	0,00121	20,13021	0,0012	20,129 ± 0,002
399,57	20,09385	0,00183	20,10121	0,00179	20,10123	0,00187	20,099 ± 0,004
400,14	20,1026	0,0015	20,10544	0,00149	20,10544	0,00151	20,104 ± 0,002
400,71	20,07634	0,0011	20,08052	0,00112	20,08052	0,0011	20,079 ± 0,002
401,29	20,07579	0,00117	20,07753	0,00119	20,07752	0,00122	20,077 ± 0,001
401,86	20,0195	9,06E-4	20,02036	0,00278	20,02036	9,697E-4	20,0201 ± 0,0005
402,43	20,02063	7,7795E-4	20,02637	8,146E-4	20,02639	7,89E-4	20,024 ± 0,003

Table 3

14th harmonic							
	25/10/2021-run1		**25/10/2021-run2**		**26/10/2021**		
$\lambda_{2\omega}$ (nm)	**E (eV)**	**σE(eV)**	**E (eV)**	**σE(eV)**	**E (eV)**	**σE(eV)**	**<E> (eV)**
399,00	21,66973	0,00107	21,67863	0,00134	21,67837	0,00122	21,676±0,005
399,57	21,63825	0,00139	21,65106	0,00125	21,65098	0,00122	21,647±0,007
400,14	21,63112	0,00122	21,63727	0,0012	21,63706	0,00108	21,635±0,003
400,71	21,57974	8,06109E-4	21,58787	8,34268E-4	21,58765	0,00131	21,585±0,005
401,29	21,55375	0,00122	21,55813	0,00123	21,55806	0,00128	21,557±0,003
401,86	21,51501	5,99424E-4	21,51816	7,13033E-4	21,51826	6,32595E-4	21,517±0,002
402,43	21,51108	9,61361E-4	21,52108	9,22541E-4	21,52158	9,75409E-4	21,518±0,006

Table 4

16th harmonic							
	25/10/2021-run1		**25/10/2021-run2**		**26/10/2021**		
$\lambda_{2\omega}$ (nm)	**E (eV)**	**σE(eV)**	**E (eV)**	**σE(eV)**	**E (eV)**	**σE(eV)**	**<E> (eV)**
399,00	24,72028	0,00867	24,73697	0,00884	24,73754	0,00884	24,73±0,01
399,57	24,66274	0,00513	24,68767	0,00521	24,68741	0,00521	24,68±0,01
400,14	24,71208	0,00561	24,72485	0,00575	24,72549	0,00575	24,721±0,008
400,71	24,63246	0,02485	24,64949	0,00588	24,65099	0,00588	24,64±0,01
401,29	24,57819	0,05365	24,58851	0,00871	24,59315	0,00871	24,587±0,008
401,86	24,59273	0,00429	24,60043	0,00431	24,60008	0,00431	24,598±0,004
402,43	24,5792	0,00496	24,59984	0,00521	24,73754	0,00521	24,59±0,01

Table 5

17th harmonic							
	25/10/2021-run1		**25/10/2021-run2**		**26/10/2021**		
$\lambda_{2\omega}$ (nm)	**E (eV)**	**σE(eV)**	**E (eV)**	**σE(eV)**	**E (eV)**	**σE(eV)**	**<E> (eV)**
399,00	26,4087	0,01765	26,44718	0,01155	26,43434	0,0074	26,43±0,02
399,57	26,37326	0,01733	26,38807	0,00806	26,39385	0,00788	26,39±0,01
400,14	26,48134	0,01097	26,48027	0,00644	26,48604	0,05491	26,483±0,003
400,71	26,38343	0,01119	26,39503	0,01039	26,39772	0,0068	26,392±0,008
401,29	26,45175	0,01654	26,5214	0,02147	26,39728	0,00984	26,46±0,06
401,86	26,16919	0,0073	26,19387	0,00546	26,18251	0,00683	26,18±0,01
402,43	26,19027	0,00802	26,21421	0,00761	26,21628	0,0074	26,21±0,01

Figures 11 - 15 show the correlation between the HHG photon energy and the wavelength of the driving photon, $\lambda_{2\omega}$(nm), for the 11th, 13th, 14th, 16th and 17th harmonics.

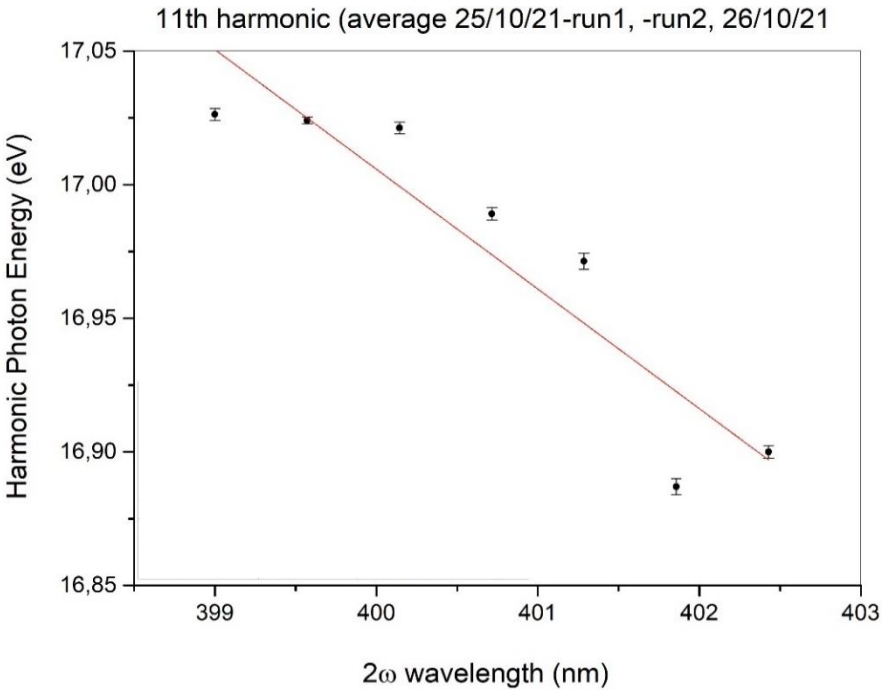

Figure 11: *Energy (three run average) of the 11th harmonic as a function of* $\lambda_{2\omega}$ (nm).

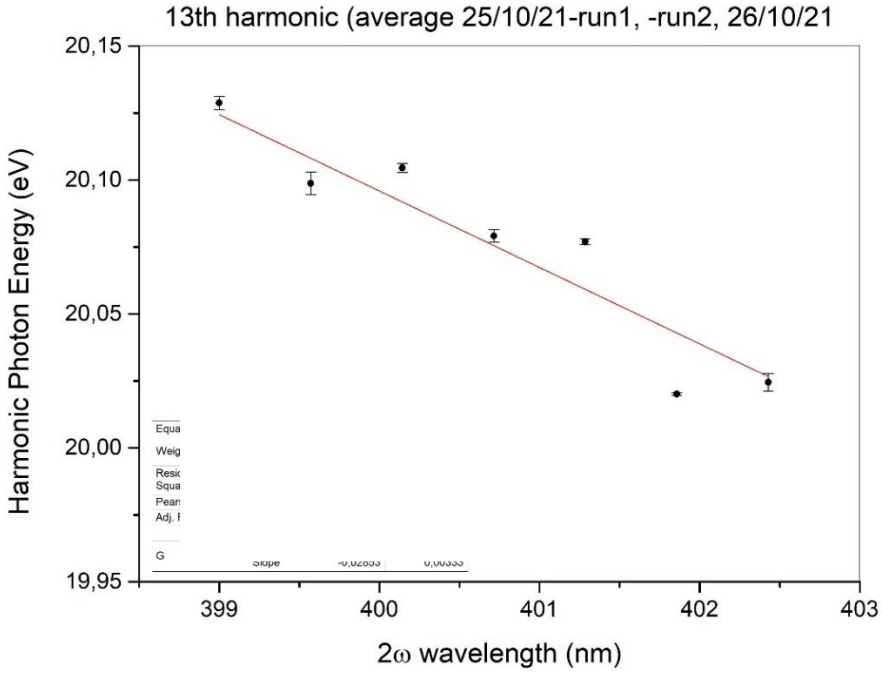

Figure 12: *Energy (three run average) of the 13th harmonic as a function of* $\lambda_{2\omega}$ (nm).

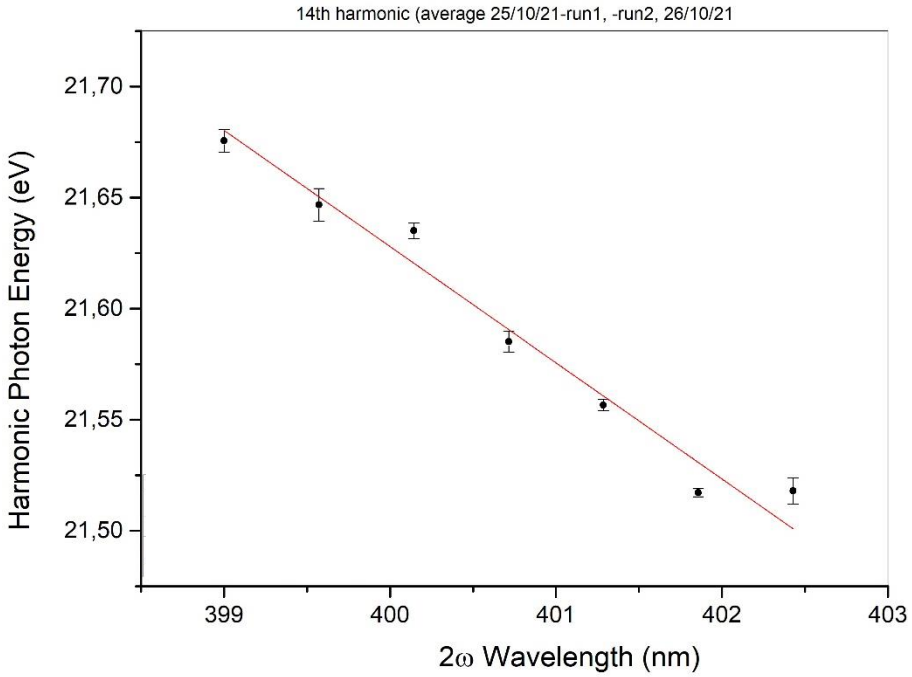

Figure 13: *Energy (three run average) of the 14th harmonic as a function of $\lambda_{2\omega}$* (nm).

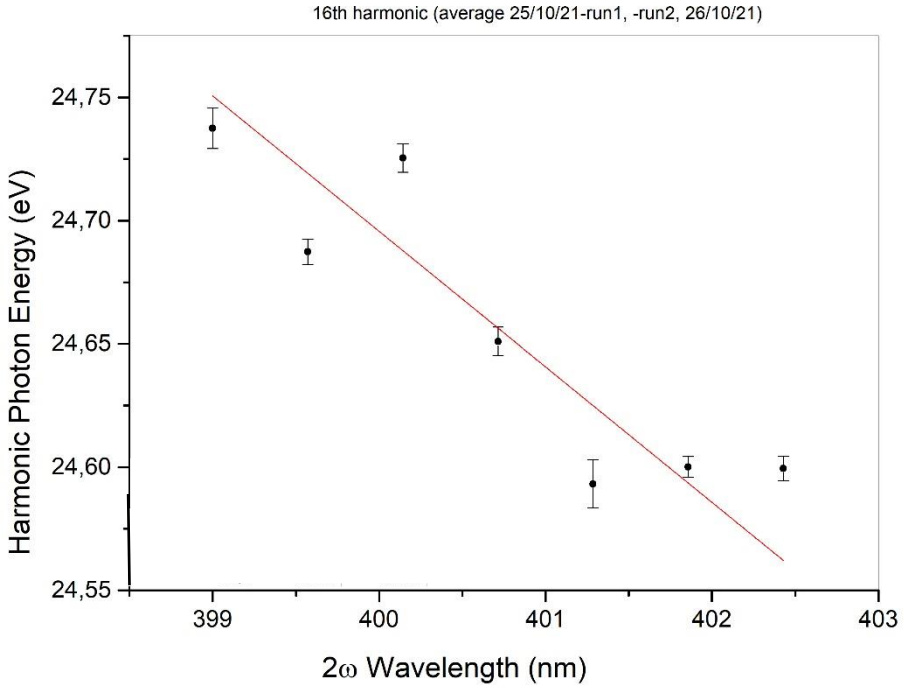

Figure 14: *Energy (three-run average) of the 16th harmonic as a function of $\lambda_{2\omega}$* (nm).

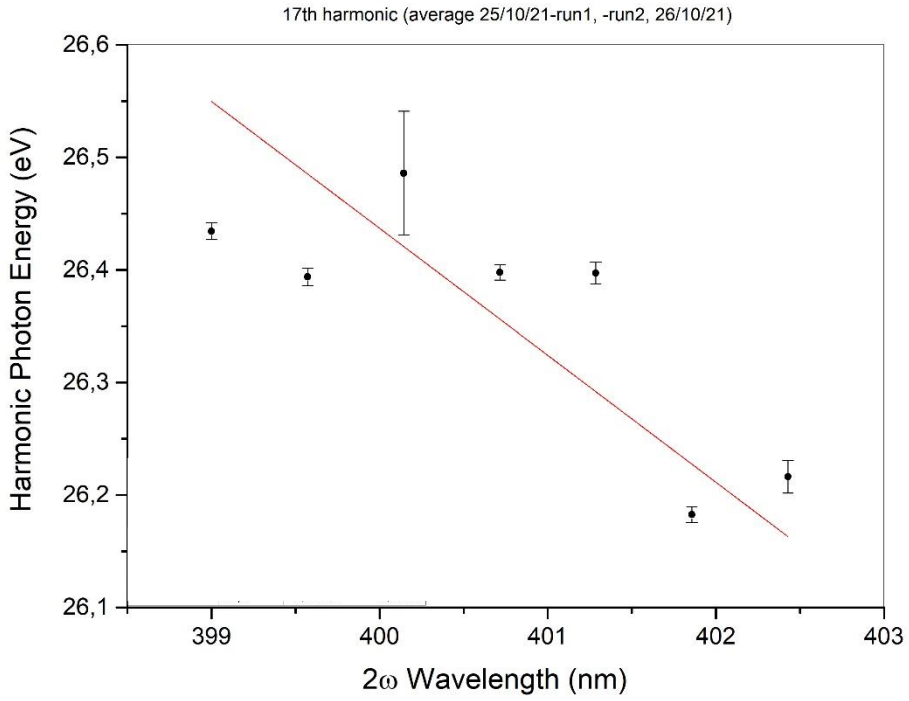

Figure 15: *Energy (three run average) of the 17th harmonic as a function of* $\lambda_{2\omega}$ (nm).

The same plots are shown in Appendix D for $E_{2\omega}$(nm) instead of $\lambda_{2\omega}$(nm). The data were fitted with a linear function, in each case. Table 6 lists the fitted slopes for the different harmonics.

Table 6

HHG order (q)	Number of Photons	Fitted slope (eV/nm)
11	4	4.6±0.7
13	4	4.0±0.6
14	5	5.6±0.4
16	5	5±1
17	6	8±3

Figure 16 shows the change of the intensity of each harmonic for the different values of $\lambda_{2\omega}$.

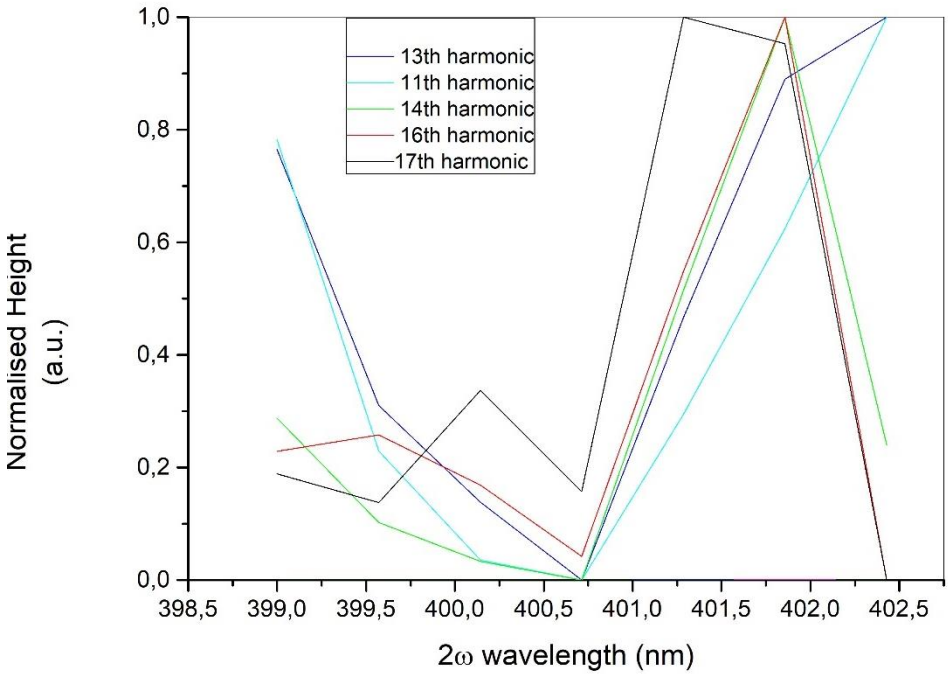

Figure 16: *The normalized heights of the harmonics 11, 13, 14, 16, 17 as a function of $\lambda_{2\omega}$ (run 26/10).*

4.2 Second experiment - measurement of degree of polarization

We obtained spectra for a series of different angles (covering several consecutive full cycles) of the polarimetric axis for three BBO orientations corresponding to $\lambda_{2\omega} = 399, 401, 403$ nm. The data were used to construct diagrams of intensity versus polarizer angle (and the corresponding polar plots) for each $\lambda_{2\omega}$ and each harmonic both for the linear and the circularly polarized HHG spectra. Here we shall show and discuss the results for the CP harmonics. A linearly polarized harmonic is also analyzed to characterize the polarizer.

The data analysis involves the interpretation of the camera output. The camera sensor is composed of millions of extremely small diodes, each of which records a pixel of the image produced by the camera lens. Each one of these pixels can be red, green or blue. When light hits a pixel, the sensor assigns a specific energy value to the pixel. From this value, the processor that is embedded in the camera can estimate the generated energy and define how dark or bright is the area captured by the lens. The combination of pixels of different colors enables the camera's computer to reproduce the shape and colors of the scene.

By measuring the harmonic yield as a function of the rotation angle, we can extract information about the step of the measurement. The maximum and the minimum value of the harmonic yield differ by 180°. The steps that correspond to the 180° are close to 22-23. So, we have approximately calculated that each step corresponds to an angle of 8°.

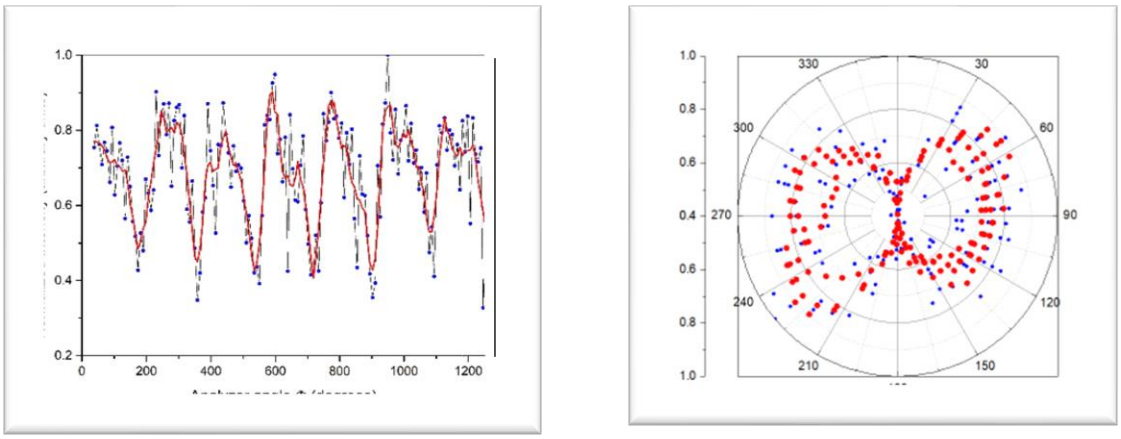

Figure 17. *Left panel*. *Dependence of normalized intensity on angle of the analyzer (in degrees) for a linearly polarized harmonic. The red line corresponds to an 8-point smoothing. Right panel. The same results shown on a polar plot. Red points represent binning over 8 data points.*

Figure 17 (left panel) illustrates the variation of the normalized intensity of the signal received by the camera for a linearly polarized harmonic as a function of the angle of rotation of the polarimeter. To produce this plot, a series of 154 images, obtained with the camera for a series of angles of rotation of the polarimeter around its axis (step), were analyzed separately, in order to derive the intensity of the harmonics of each spectrum for every step. The right panel of Figure 17 shows the same data depicted on a polar plot.

Similar plots (normalized to unit intensity) were constructed for the CP harmonics 10^{th}, 11^{th}, 13^{th} and 14^{th}, and for $\lambda_{2\omega}$ 399, 401 and 403nm. The corresponding (normalized to unity) polar plots are shown in Figure 18.

The periodic modulation with the angle of rotation of the polarizer, shown on the left panel of Fig. 17 is a manifestation of the generalized Malus law, as explained in Appendix B. For an ideal polarizer and circularly polarized light no intensity modulation is expected. On the other hand for linearly polarized light one expects the intensity to become zero at right angles to the polarization axis. The **contrast**, i.e. the ratio of the maximum to the minimum intensity in such plots, is related to the polarization state of the incident light. For an *ideal polarizer* and *linearly* polarized light, $I_{min} = 0$ and the contrast is not defined. For an ideal polarizer and *circularly* polarized light, the contrast is equal to 1, as all directions of the electric field are equivalent. For a ***non-ideal polarizer***, the value of the contrast corresponding to *linear* polarization needs to be experimentally determined. Using Fig. 16, we found this value to be equal to 1.8 in our case. Therefore, depending on the state of polarization of the HHG, we expect the measured contrast to range from ~1 for circular polarization to ~1.8 for linear polarization.

The **polar plots** (right panel of Fig. 17 and Fig. 18) are a different way to visualize the intensity modulation with polarization angle. Circular polarization corresponds to a circular polar plot, while linear polarization to an eight-shaped line. Elliptically polarized light yields shapes in between these.

The plots of Figure 18 indicate that for all values of $\lambda_{2\omega}$, the high harmonics (10, 11, 13 and 14) generated by the bicircular driving field show elliptical polarization. This is better quantified by calculating the **ellipticity** based on the contrast values, using the equations presented in

Appendix B. More specifically, for each case presented in Fig. 18, the experimental dependence of intensity on the polarizer angle (i.e. from plots similar to the left panel of Fig. 17) was fitted with the generalized Malus law (see Appendix B). The resulting fits are shown with the red continuous lines on the polar plots of Fig. 18. Table 7 summarizes the measurements of contrast and resulting ellipticity values. The contrast values obtained range between ~1.2 and ~1.6 with an average of 1.37±0.14, clearly indicating elliptical polarization. The fitted ellipticities range from 0.4 to 0.9 with an average of 0.56±0.14. For circular polarization one expects both the contrast and the ellipticity to be ~1. As we move to linearly polarized light, the contrast increases (to values as low as 1.6) and the ellipticity decreases to values as low as 0.4 (see Fig. 19).

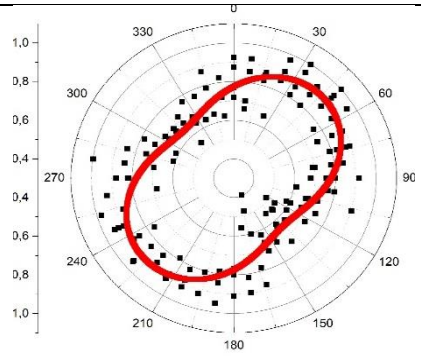	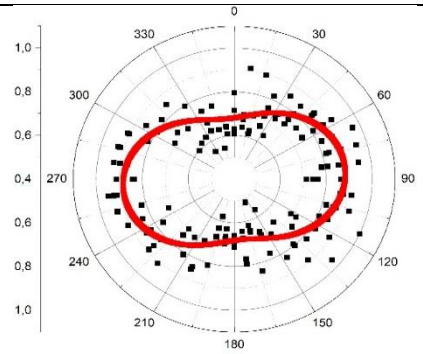
$\lambda_{2\omega}$=399nm, 10th harmonic	$\lambda_{2\omega}$=401nm, 10th harmonic
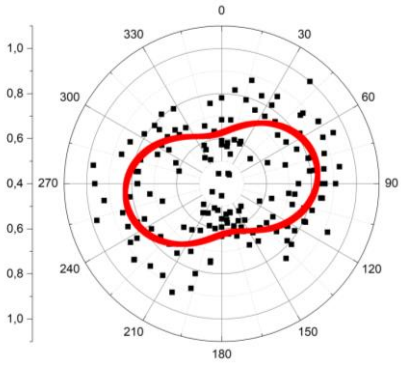	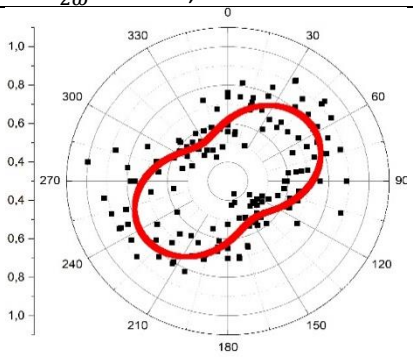
$\lambda_{2\omega}$=403nm, 10th harmonic	$\lambda_{2\omega}$=399nm, 11th harmonic
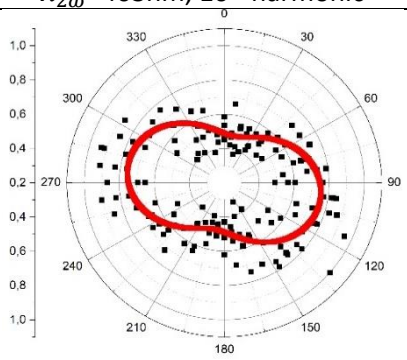	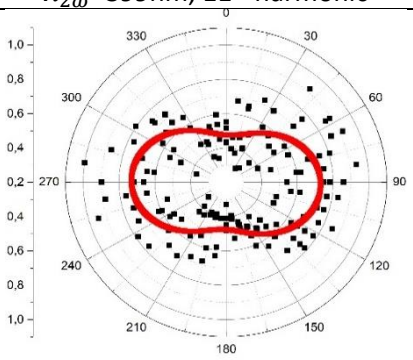
$\lambda_{2\omega}$=401nm, 11th harmonic	$\lambda_{2\omega}$=403nm, 11th harmonic

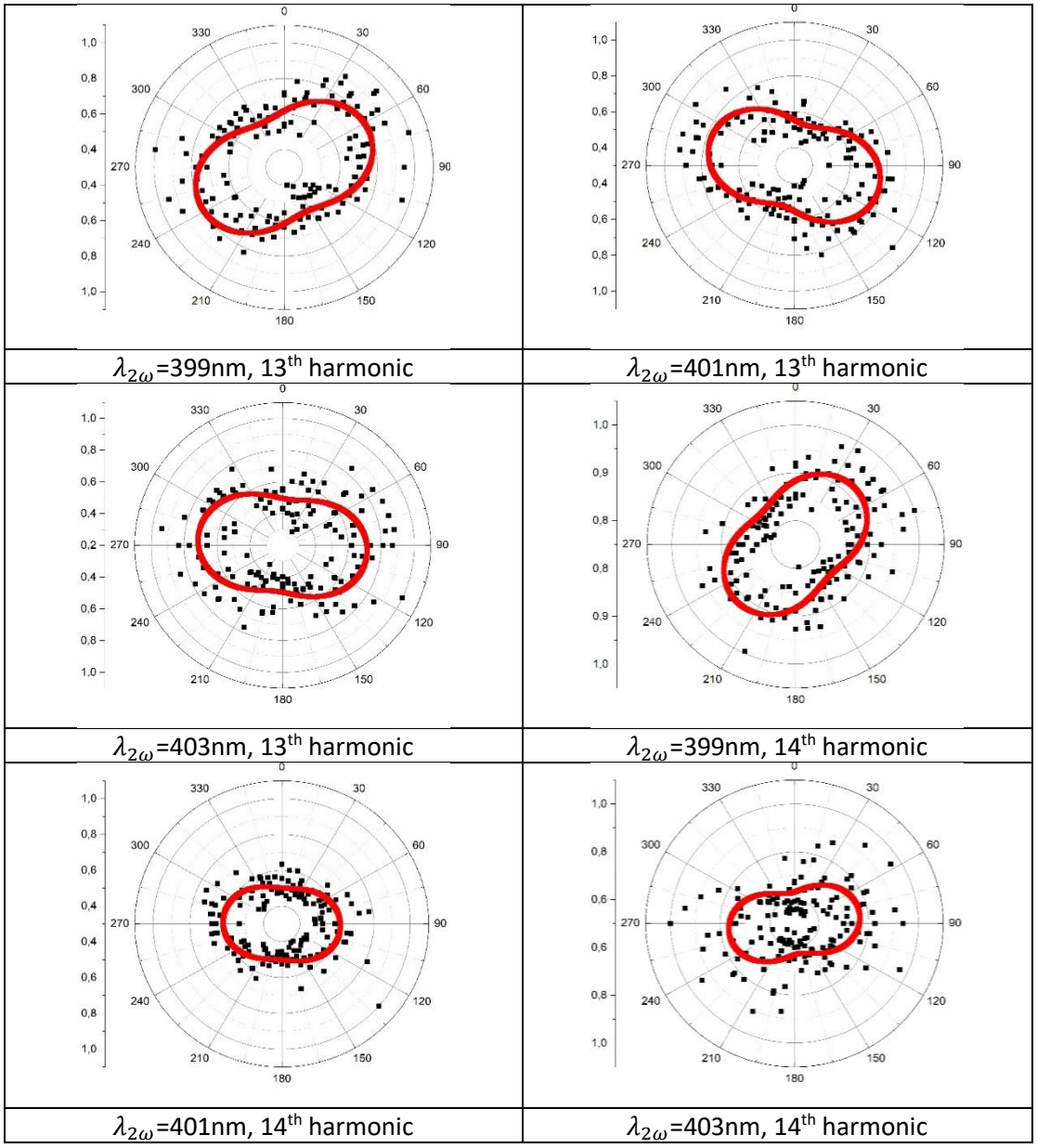

Figure 18. *Normalized polar plots of the intensity as a function of polarization angle (black points). The red lines are derived from fitting the data points with the generalized Malus law.*

Table 7. Contrast and ellipticity of the CP HHG

$\lambda_{2\omega}$(nm)	Harmonic Order	Contrast	Ellipticity
399	10	1.40	0.53±0.05
	11	1.51	0.43±0.04
	13	1.39	0.54±0.05
	14	1.09	0.87±0.09
401	10	1.30	0.62±0.06
	11	1.58	0.40±0.04
	13	1.45	0.50±0.05
	14	1.24	0.69±0.07

403	10	1.33	0.58±0.06
	11	1.53	0.40±0.04
	13	1.45	0.50±0.05
	14	1.22	0.72±0.07

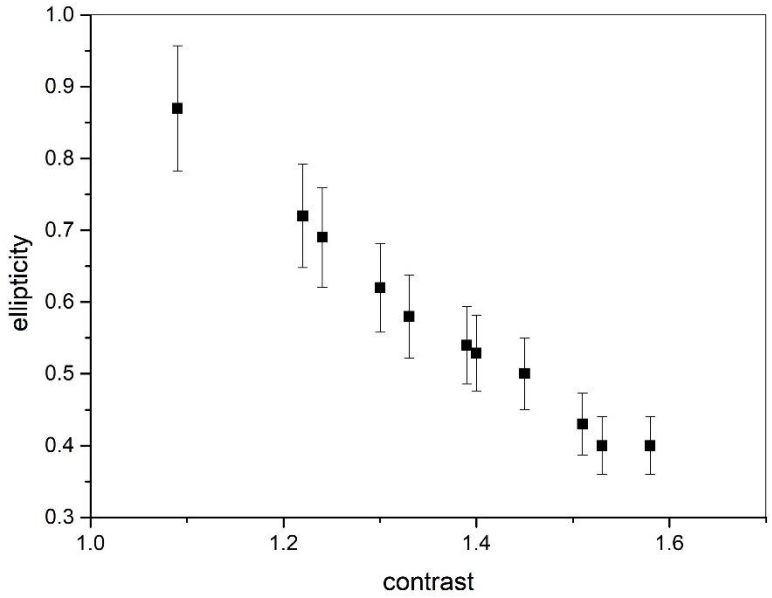

Figure 19. *The derived ellipticity values versus the contrast, for the data of Table 7. This behavior is as expected (Appendix B)*

Figure 20 shows the dependence of ellipticity on harmonic order (left panel) and on the driving field wavelength (right panel). Given the errors, no significant trends can be identified.

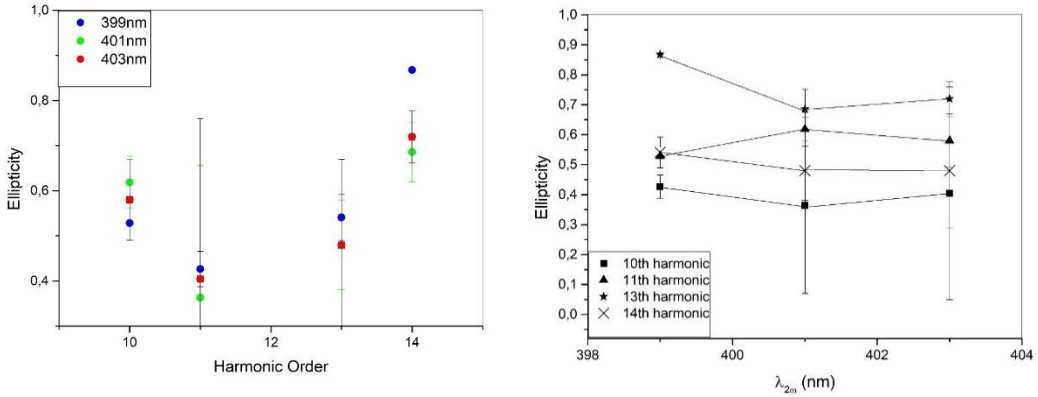

Figure 20. *Left panel. The dependence of derived ellipticity on harmonic order. Right panel. The dependence of ellipticity on driving field wavelength*.

From the HHG spectra obtained for the three different values of $\lambda_{2\omega}$, shown in Figure 21, we could confirm the spectral shifts for different values of $\lambda_{2\omega}$ that were measured in the first experiment (paragraph 4.1) using the TOF-spectrometer. For example, the energy difference measured for the 13^{th} harmonic for $\lambda_{2\omega}$ =399nm and 403nm is estimated to be ~150meV, similar to the result of experiment 1.

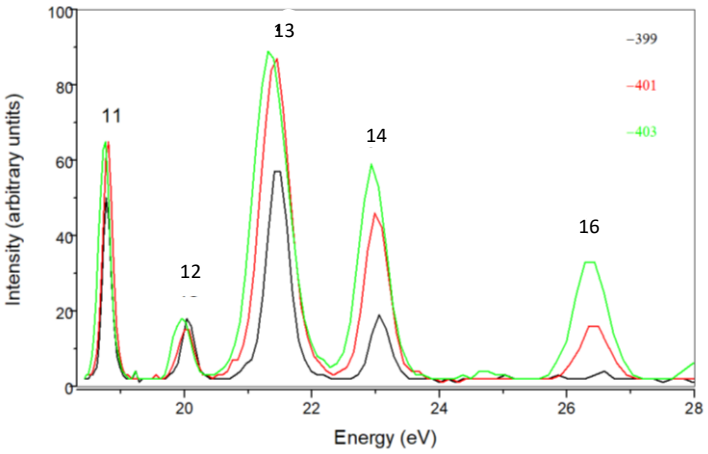

Figure 21. The HHG spectra obtained with the grating spectrograph for three values of $\lambda_{2\omega}$.

5. Interpretation of results

5.1 Main features of the observed spectra

5.1.1 Orders of observed harmonics

The harmonics produced by the bicircular field are expected to have orders $3m+1$ and $3m-1$. Those with $q=3m+1$ have photon helicity corresponding to left circularly polarized (LCP) field, while those with $q=3m-1$ have opposite helicity, corresponding to right circularly polarized (RCP) field (Vassakis et al. 2021, Kfir et al. 2015, 2016 and Appendix A). The latter holds for a laser beam whose laser field components are a left-rotating circularly polarized field with fundamental frequency ω and a right-rotating circularly polarized field with second harmonic frequency 2ω. If the helicities of the laser field components are opposite, then spin angular momentum conservation dictates that each generated harmonic will possess helicities opposite to the ones described above.

For $m=4$ the harmonics produced are the 11th (RCP) and the 13th (LCP), at energies 17.05eV and 20.15eV, respectively. These peaks are easily recognized in the spectra. For $m=5$, we expect the 14th (RCP) and 16th (LCP) harmonics, at 21.7eV and 24.8eV, while for $\mathrm{m}=6$, we expect the 17th (RCP) and 19th (LCP) harmonics, at 26.35eV and 29.45eV, and so on.

These predictions are confirmed by the recorded spectra: They all (see Fig. 6 for examples) show peaks that correspond to the harmonics 11, 13, 14, 15, 16, and 17, with energies ranging from about 17 to about 26eV.

We would expect to observe higher order harmonics, according to the cutoff law, which predicts that for equal intensities, $\mathrm{E}_{max}=1.2I_{\mathrm{p}}+(1/\sqrt{2})3.17U_p$ (Milošević, et al., 2000), where U_p is the ponderomotive energy given by eq. 6 of section 2. The above cut-off law can be used only if the laser intensities of the two field components are equal.

Here, $U_p=U_{p\omega}+U_{p2\omega}$ with $I_\omega\approx I_{2\omega}\approx 10^{14}\mathrm{W/cm^2}$. So, $U_{p\omega}=5.971eV$, $U_{p2\omega}=1.485eV$, therefore, $U_p=7.456eV$ and $\mathrm{E}_{max}=1.2\times 15.76eV+(1/\sqrt{2})\times 3.17\times 7.456\mathrm{eV}=35.628\mathrm{eV}$, which corresponds to the 23rd harmonic (E_{23} =12x1.55eV=35.65eV). The fact that we observe fewer harmonics may be caused by a combination of effects. The main one is the reduced efficiency of the detecting system at higher energies. Another possible reason is that the macroscopic response of the medium and the conditions for selective phase matching depend on the location of the focus and of the nozzle from which the Ar gas is injected into the chamber (Kfir et al., 2016, Milošević et al. 2001).

5.1.2 Intensities of observed harmonics

As can be seen in the spectra of Fig. 6, the 13th harmonic ($q=3m+1$ for $m=4$) is significantly more intense than the 11th harmonic ($q=3m-1$ for $m=4$). The former is LCP and the latter RCP. This behavior is expected theoretically. It has been demonstrated in Kfir et al. (2016) that when e.g. LCP is well matched then RCP will show non-negligible phase mismatch (see Appendix A for details). This difference in intensity is not that clear for the harmonics 14th and 16th ($q=3m-1$ and $q=3m+1$, for $m=5$), but part of the problem may be the lower sensitivity at higher energies.

5.2 Energy shift and intensity change of HHG with rotation angle of the BBO crystal

One of the objectives of the conducted experiment was to investigate the effect on the HHG spectra of different angles of rotation of the BBO crystal around its optical axis. The different angles lead to a shift in the central frequency of the driving pulse. The most obvious effect is an HHG energy shift (figures 11-15). As presented in detail in Appendix A, the energy of the HHG of order *q* is given by

$\hbar\omega_q = \hbar l\omega_1 + \hbar m\omega_2$, where $l = (m \pm 1)$

The term $l\hbar\omega_1$ remains constant, since $\hbar\omega_2$ is changed with the angle of rotation (as ω_2 changes). Therefore $\hbar\omega_q$ is a linear function of $\hbar\omega_2$ with a slope equal to m. From the values of the slopes given in Table 6, it is confirmed that within the errors the slope is indeed equal to m, in all cases.

As shown in Figure 16, the intensity of the HHG depends on the rotation angle of the BBO crystal, with the angles corresponding to $\lambda_{2\omega} \approx 401.5 - 402nm$ giving the highest intensities for all visible harmonics, which means that in the direction in which the $\lambda_{2\omega} \approx 401.5 - 402nm$ wavelengths are generated, the best phase-matching is achieved.

5.3 Presence of the 15th harmonic in the spectra

In all HHG spectra obtained, there is a weak line around 23.25eV, which corresponds to the 15th harmonic ($q = 3m$, for $m = 5$). The 3m harmonics are theoretically forbidden, due to the three-fold symmetry of the bicircular field. However, if there is a slight ellipticity in the (ω and 2ω) driving fields, this three-fold symmetry is broken, leading to the production of 3m harmonics. Such ellipticity can be caused if the retardation and crystal axes of the QWP diverge from the ideal case (Vassakis et al. 2021, Jiménez-Galán et al. 2017). On the other hand, 3m harmonics can also occur even for perfectly circularly polarized pulses (Vassakis et al., 2021, Jiménez-Galán et al., 2017, Barreau et al., 2018). It was shown by Jiménez-Galán et al. (2017) that when the second harmonic either precedes or is more intense than the fundamental field, the weak effects of dynamical symmetry breaking caused by finite pulse duration are amplified by electrons trapped in Rydberg orbits and thus forbidden harmonic lines are produced. In our case, measurement of the polarization of the driving fields might help determine whether ellipticity is the main cause of the appearance of the forbidden 15th harmonic in our spectra. Finally, another less likely cause for the appearance of the forbidden 15th harmonic is a possible anisotropy of the HH generating medium, however this is minimized by the use of noble gases (here Ar) and by the colinear geometry of the MAZEL-TOV apparatus (Vassakis et al. 2021, Baykusheva et al. 2016, Yuan & Bandrauk 2018).

5.4 Polarimetric results

The measurement of the state of polarization of the HHG spectrum that was achieved with the second experiment showed highly elliptical polarization. For an ideal system, theory predicts circular polarization for the $3m + 1$ and $3m - 1$ harmonics, which is close to the experimental result. No statistically significant change of ellipticity was seen for the different values of $\lambda_{2\omega}$ nor for the different harmonic orders.

6. Conclusions

In the present thesis we characterized spectroscopically and polarimetrically the spectrum of high harmonics generated by the interaction of a femtosecond bicircular (800nm and 400nm) counter-rotating laser field with Argon gas. HHG spectra were analyzed for different angles of the BBO crystal providing small shifts in the $\lambda_{2\omega}$ component. The main conclusions of the study can be summarized as follows:

(i) The harmonics produced by the bicircular field had orders corresponding to $3m + 1$ and $3m - 1$, as theoretically expected (11^{th}, 13^{th}, 14^{th}, 16^{th} and 17^{th}). Fewer harmonics were observed than allowed by the cutoff law, due to the reduced efficiency of the detecting system at higher energies and due to the reduced efficiency in phase-matching.

(ii) The intensities of the harmonics corresponding to $q = 3m + 1$ have higher intensities than their $3m - 1$ counterparts, for $m = 4$, while this difference is less evident or diminished for $m = 5$.

(iii) The spectra also show the 15^{th} harmonic which is not expected for an ideal bi-circular field. However, if there is a slight ellipticity in the (ω and 2ω) driving fields, the three-fold symmetry of the bicircular field is broken.

(iv) The intensity of the harmonics depends on the rotation angle of the BBO crystal, with the angles corresponding to $\lambda_{2\omega} \approx 401.5 - 402nm$ giving the highest intensities. So, the intensity of the HHG spectrum can be optimized in this way. The energy shifts of the HHG for different BBO angles are as expected from the change in the photon energy of the driving photons.

(v) The measurement of the state of polarization of the HHG spectra confirmed highly elliptical polarization, with no clear dependence on harmonic order or BBO angle of rotation.

References

Barreau, L., Veyrinas, K., Gruson, V., et al., Evidence of depolarization and ellipticity of high harmonics driven by ultrashort bichromatic circularly polarized fields. *Nat. Commun.* , 9, 4727, 2018

Baykusheva, D., Ahsan, M., Lin, N., Wörner, H., Bicircular High-Harmonic Spectroscopy Reveals Dynamical Symmetries of Atoms and Molecules, *Phys. Rev. Lett*., 116, 123001, 2016

Corkum, P. B., Plasma perspective on strong-field multiphoton ionization, *Phys. Rev. Lett*., 71(13), p1994, 1993

Damian, I., 2004, Buletinul Stiintific al Universitatii Politehnica din Timisoara, tom 49(63), 2, p. 107, Matematica-Fizica, arXiv:physics/0604073 [physics.ed-ph]

Eichmann, H., Egbert, A., Nolte, S., Momma, C., Wellegehausen, B., Becker, W., Long, S. and McIver, J. K., *Phys. Rev. A*, 51, R3414, 1995

Ferray, M., L'Huillier, A., Li, X. F. , Lompré, L. A. , Mainfray, G. and Manus, C.. Multiple-harmonic conversion of 1064 nm radiation in rare gases*, Journal of Physics B,* 21, L31, 1988

Ferré, A., Handschin, C., Dumergue, M. et al, A table-top ultrashort light source in the extreme ultraviolet for circular dichroism experiments, *Nature Photon* 9, 93, 2015

Fleischer, A., Sidorenko, P., Cohen, O., Generation of high-order harmonics with controllable elliptical polarization, *Opt. Lett. OSA*, 38, 223, 2013

Frank, F., Generation and Application of Ultrashort Laser Pulses in Attosecond Science, *PhD Thesis*, Physics Department, Imperial College London, 2011

Gontier, Y. and Trahin, M., Energetic electron generation by multiphoton absorption, *J. Phys. B: Atom. Mol. Phys.,* 13**,** 4383, 1980

Hickstein, D., Dollar, F., Grychtol, P. et al., Non-collinear generation of angularly isolated circularly polarized high harmonics, *Nature Photon*., 9, 743, 2015

Jiménez-Galán, A., Zhavoronkov, N., Schloz, M., Morales, F., Ivanov, M., Time-resolved high harmonic spectroscopy of dynamical symmetry breaking in bi-circular laser fields: the role of Rydberg states, *Opt. Expr.,* 25, 22880, 2017

Kfir, O., Grychtol, P., Turgut, E., Knut, R., Zusin, D., Popmintchev, D., Popmintchev, T., Nembach, H., Shaw, J.M., Fleischer, A., Kapteyn, H., Murnane M. and Cohen, O., Generation of bright phase-matched circularly polarized extreme ultraviolet high harmonics, *Nature Photonics*, 9, 99, 2015

Kfir, O., Grychtol, P., Turgut E., Knut R., Zusin D., Fleischer A., Bordo E., Fan T., Popmintchev D., Popmintchev T., Kapteyn H., Murnane M. and Cohen, O., Helicity-selective phase-matching and quasi-phase matching of circularly polarized high-order harmonics: towards chiral attosecond pulses, *J. Phys. B: At. Mol. Opt. Phys.*, 49, 123501, 2016a

Kfir, O., Bordo, E., G. Ilan Haham, O. Lahav, A. Fleischer and O. Cohen, In-line production of a bi-circular field for generation of helically polarized high-order harmonics, *Appl. Phys. Lett.*, 108, 211106, 2016b

Khademian, A., Theoretical Study of Second Harmonic Generation of a Blue Laser at 486 nm Using a BBO Crystal in a Standing Wave Buildup Cavity. *Master of Science* (Physics), May 2002

Kulander, K. C., Schafer K. J. and Krause, J. L., Dynamics of short-pulse excitation, ionization and harmonic conversion, In "*Super-Intense Laser-Atom Physics*", Plenum Press, New York, 1993

Lambert, G., Vodungbo, B., Gautier, J. et al., Towards enabling femtosecond helicity-dependent spectroscopy with high-harmonic sources, *Nat Commun,* 6, 6167, 2015

Le A.-T., Wei, H., Jin C., Lin, C.D., Strong-field approximation and its extension for high-order harmonic generation with mid-infrared lasers, *J. Phys. B: At. Mol. Opt. Phys*., 49, 2016

Lewenstein, M., Balcou, Ph., Ivanov, M. Yu., L'Huillier, A. and Corkum, P. B., Theory of high-harmonic generation by low-frequency laser fields, *Phys. Rev. A*, 49, 2117, 1994

Long, S., Becker, W., McIver, J.K., Model calculations of polarization-dependent two-color high-harmonic generation, *Phys. Rev. A*, 52, 2262, 1995

Long, Z. J. and Liu, W-K, Keldysh theory of strong-field ionization, *Canadian Journal of Physics*, Vol. 88, No.4, 2010

Maiman, T.H., Stimulated Optical Radiation in Ruby, *Nature*, 187**,** 493–494, 1960

Makos, I., Orfanos, I., Nayak, A. et al. ,A 10-gigawatt attosecond source for non-linear XUV optics and XUV-pump-XUV-probe studies, *Sci Rep* 10**,** 3759, 2020

McPherson, A., Gibson, G., Jara, H., Johann, U., Luk, T.S., McIntyre, I.A., Boyer K. and Rhodes, C. K., Studies of multiphoton production of vacuum ultraviolet radiation in the rare gases, *Journal of the Optical Society of America B*, 4, 595, 1987

Milošević, D.B., & Becker, W., Attosecond pulse trains with unusual nonlinear polarization, *Phys. Rev. A*, 62, 011403, 2000

Milošević, D., Becker, W. , and Kopold, R., Generation of circularly polarized high-order harmonics by two-color coplanar field mixing, *Phys. Rev. A.*, 61. 063403, 2000

Milošević, D.B., Becker, W., Kopold, R., Sandner, W., High-harmonic generation by a bichromatic bicircular laser field, *Laser Physics*, 11, 165, 2001

Milošević, D.B., Circularly polarized high harmonics generated by a bicircular field from inert atomic gases in the p state: A tool for exploring chirality-sensitive processes, *Phys. Rev. A*, 92, 043827, 2015

Orfanos, I., Development and characterization of an intense attosecond pulse source for XUV-pump-XUV-probe experiments, *PhD Thesis*, Physics Department, University of Crete, 2020

Papazoglou, D., 2021, "Wave Optics and Optical Metrology, MSc course, Lecture Notes

Popmintchev, T., Chen, M.-C., Bahabad, A., Gerrity, M., Sidorenko, P., Cohen, O., Christov, I.P., Murnane, M.M. and Kapteyn, H.C., Phase matching of high harmonic generation in the soft and hard x-ray regions of the spectrum, *Proc. Nat. Acad. Sci. USA*,106, 10516, 2009

Popmintchev, T., Chen, M.-C., Arpin P., Murnane, M.M. and Kapteyn, H.C., The attosecond nonlinear optics of bright coherent x-ray generation, *Nat. Photon*., 4, 822, 2010

Popov, V.S., Tunnel and multiphoton ionization of atoms and ions in a strong laser field (Keldysh theory), *Physics-Uspekhi* , 47, 855, 2004

Protopapas, M., Keitel, C. H., and Knight, P. L., Atomic physics with super-high intensity lasers, *Reports on Progress in Physics*, 60, no. 4, pp. 389, 1997

Skantzakis, E., Generation and applications of intense isolated attosecond pulses, *PhD Thesis*, University of Crete, 2011

Skantzakis, E., Chatziathanasiou, S., Carpeggiani, P. et al. Polarization shaping of high-order harmonics in laser-aligned molecules, *Sci Rep*, 6, 39295, 2016

Strickland, D., & Mourou, G., Compression of amplified chirped optical pulses, *Optics Commun*., 55, 447, 1985

Vassakis, E., Orfanos, I., Liontos, I., Skantzakis, E. Generation of Energetic Highly Elliptical Extreme Ultraviolet Radiation, *Photonics,* 8, 378, 2021

Weber, A., Böning, B., Minneker, B., and Fritzsche, S., Generation of elliptically polarized high-order harmonic radiation with bi-elliptical two-color laser beams, *Phys. Rev. A*, 104, 063118, 2021

Woehlecke, M., Betzler, K., Imlau, M., Lecture notes, Nonlinear Optics, University of Osnabrueck, 2005

Yanovsky, V., Chvykov, V., Kalinchenko, G., Rousseau, P., Planchon, T., Matsuoka, T., Maksimchuk, A., Nees, J., Cheriaux, G. , Mourou, G. , and Krushelnick, K., Ultra-high intensity- 300-TW laser at 0.1 Hz repetition rate, *Opt. Express*, 16, 2109, 2008

Yuan, K.J., Bandrauk, A.D., Symmetry in circularly polarized molecular high-order harmonic generation with intense bicircular laser pulses, *Phys. Rev. A*, 97, 023408, 2018

Appendix A

Phase-matching of circularly polarized high order harmonics (Detailed Proof of relations)

When a bi-circular field composed of two co-propagating counter-rotating fields with frequencies ω_1 and ω_2, drives the circularly polarized high harmonic generation, the following conservation laws are obeyed:

energy conservation $\omega_q = l\omega_1 + m\omega_2$ (A.1)

Orbital Angular Momentum conservation (to get CP) $l = m \pm 1$ (A.2)

linear momentum conservation $\boldsymbol{k}_q = l\boldsymbol{k}_1 + m\boldsymbol{k}_2$ (A.3)

for collinear beams, eq. A.3 reduces to $k_q = lk_1 + mk_2$ (A.4)

parity conservation $l + m$ is odd (A.5)

Spin Angular Momentum conservation $\sigma^{(0)}_{(n_1,n_2)} = l\sigma_1 + m\sigma_2$ (A.6)

where $\omega_q = q\omega_1$ is the frequency of the generated harmonic of order q, and l and m are the number of photons of frequencies ω_1 and ω_2, respectively, that contribute to the creation of the HH photon, ω_q. If the ratio ω_2/ω_1 is an integer, so is the HH order q (Kfir et al. 2016a). Eq. (A.1), (A.3) and (A.4) are self-evident. Eq. (A.2) indicates that the circularly polarized HHG photon has the spin of the one extra photon ($+1$ for a left circularly polarized photon, and -1 for a left circularly polarized photon). In Eq. (A.6) σ_1 and σ_2 are the spin expectation values of the emitted HHG photon generated by a combination of photons of frequency ω and 2ω respectively. The following figure depicts the conservation laws described by the above equations.

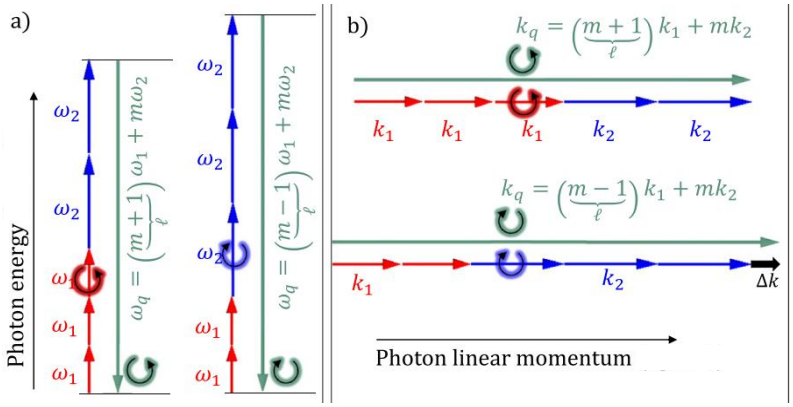

Figure A1 *Depiction of the conservation laws described by eq. A1 and A4, for* $l = 3$ *and* $m = 2$ *and* $l = 2$, $m = 3$, *as an example. (a) Conservation of energy, for the two cases (* $l = m \pm 1$); *(b) Phase (momentum) matching depends on spin, i.e. if e.g. LCP is well matched, then RCP will show a non-negligible phase mismatch Δk (reproduced from Kfir et al. 2016α, their fig. 2).*

The momentum of the HH photon, k_q, is determined by the momenta of the pump photons annihilated to create it, i.e. of l photons of momentum k_1 and m photons of momentum k_2. The so-called **full** phase matching condition is dictated by the conservation of momentum. However, because of the chromatic dispersion in the material, the fields with frequencies ω_1 and ω_2 have different refractive indices, and thus $\frac{k_2}{k_1} \neq \frac{\omega_2}{\omega_1}$. This leads to a phase (or momentum) mismatch, Δk, which can be derived from eq. A.1 and A.4,

$$\Delta k = l\mathrm{k}_1 + mk_2 \text{ - } k_q = l\frac{\omega_1}{c}\Delta n_1 + m\frac{\omega_2}{c}\Delta n_2 \quad \text{(A.5)}$$

using $n = c/v \ and \ v = \omega/k \Rightarrow \Delta k = (\Delta n)\omega/c)$

where $\Delta n_{1,2} = n_{1,2} - n_q$, with $n_{1,2}$ being the refractive indices of the crystal for the frequencies ω_1 and ω_2 respectively, and n_q for the HH ω_q.

Thus Eq. (A.5) gives the phase mismatch for the generation of circularly polarized high harmonic photons of frequency $\omega_q = l\omega_1 + m\omega_2$, with $l = m \pm 1$ (eq. A. 2).

For phase matching $\Delta k = 0$, and hence from Eq. (A.5) we get the phase matching condition:

$$\frac{\omega_2 \Delta n_2}{\omega_{1\Delta n_1}} = -\frac{l}{m} = -\frac{m \pm 1}{\mathrm{m}} \quad \text{(A.6)}$$

Eq. (A.6) implies that Δn_1 and Δn_2 have opposite signs. This has important implications for the phase mismatching for HHG of different helicity.

For specific dispersion terms $\Delta n_{1,2}$ it is clear that full phase matching can occur only for one harmonic, say *q*, for which condition (A.6) holds.

Let us consider the next harmonic generated with the **same spin** as the *q* harmonic, then the phase mismatch will be given by eq. (A.5) :

$$\Delta k' = l'\frac{\omega_1}{c}\Delta n_1 + m'\frac{\omega_2}{c}\Delta n_2 \quad \text{(A.7)}$$

where

$$m' = m + 1 \ \text{και} \ l' = m' + 1 = m + 2 = l + 1 \quad (\text{for} \quad l = m + 1) \quad \text{(A.8)}$$

From (A.6), (A.7) and (A.8) we derive:

$$\Delta k' = l'\frac{\omega_1}{c}\Delta n_1 + m'\frac{\omega_2}{c}\Delta n_2 = (l+1)\frac{\omega_1}{c}\Delta n_1 + (m+1)\frac{\omega_2}{c}\Delta n_2 \underset{A.6}{\Rightarrow}$$

$$\Delta \mathrm{k}' = \frac{\omega_1}{c}\Delta n_1 + \frac{\omega_2}{c}\Delta n_2 \quad \text{(A.9)}$$

The value of Δk' is small since Δn_1 and Δn_2 have opposite signs.

Let us now consider the case where $m' = m + 1 \ \text{και} \ l' = m'' - 1 = m = l - 1$. i.e. the harmonic is counter-rotating. In this case

$$\Delta k' = l'\frac{\omega_1}{c}\Delta n_1 + m'\frac{\omega_2}{c}\Delta n_2 = (l-1)\frac{\omega_1}{c}\Delta n_1 + (m+1)\frac{\omega_2}{c}\Delta n_2 \underset{A.6}{\Rightarrow}$$

$$\Delta k' = -\frac{\omega_1}{c}\Delta n_1 + \frac{\omega_2}{c}\Delta n_2 \quad \text{(A.10)}$$

which is usually much larger than (A.9), as both terms are positive.

As $\Delta n_1 \sim -\Delta n_2$, we van approximate the phase mismatch in this case by

$$\Delta k' \cong -2\frac{\omega_1}{c}\Delta n_1 \quad \text{(A.11)}$$

We conclude that in the example of Fig. A1, co-rotating harmonics ($l = m + 1$) are better phase matched than the counter-rotating ones ($l = m - 1$).

The expected energies of the LCP and RLP harmonics

The right circularly polarized (RCP) harmonics (spin -1) correspond to the case $l = m - 1$ of eq. (A.2), hence, according to eq. (A.1), they have frequencies given by

$$\omega_q = (m-1)\omega_1 + m\omega_2 \quad (\text{A.12})$$

The left circularly polarized (LCP) harmonics (spin $+1$) correspond to the case $l = m + 1$ of eq. (A.2), hence, according to eq. (A.1), they have frequencies given by

$$\omega_q = (m+1)\omega_1 + m\omega_2 \quad (\text{A.13})$$

For $\omega_2 = 2\omega_1$, eq. (A.12) gives $\omega_q = (3m-1)\omega_1$ (A.14) for the RCP harmonics and eq. (A.13) gives $\omega_q = (3m+1)\omega_1$ (A.15), for the LCP harmonics.

The above are valid, if the component of the bicircular field with frequency 2ω is rotating in the counter-clockwise sense (LCP) and the component of the bicircular field with frequency ω is rotating in the clock-wise sense (RCP). In the opposite case, the harmonic with $\omega_q = (3m+1)\omega_1$ is rotating in the same direction as the RCP driving field component of frequency 2ω, while the harmonic with frequency $\omega_q = (3m-1)\omega_1$ is LCP and follows the rotation of the driving field component of frequency ω, which is counter-clockwise.

Appendix B

Polarization - Reflective polarizer - Proof of equations used

With the XUV polarimeter, we measured the ellipticity of the highly elliptical XUV radiation produced through HHG, in order to characterize the XUV light. The analysis of the polarization state of the incident light is achieved via a EUV reflective polarization analyzer, which functions as a non-ideal linear polarizer/analyzer.

The polarization of light and its control are often described using Jones vectors and matrices. Jones vectors describe the polarization state of light. Jones matrices describe the effect of different optical devices and processes on the polarization state. They are operators that act on the incoming Jones vector and produce the outcoming Jones vector.

The electric field of a monochromatic (of angular frequency ω) plane electromagnetic wave propagating along the z axis can be written as

$$\begin{pmatrix} E_x(t) \\ E_y(t) \\ 0 \end{pmatrix} = \begin{pmatrix} E_{0x}e^{i(kz-\omega t+\phi_x)} \\ E_{0y}e^{i(kz-\omega t+\phi_y)} \\ 0 \end{pmatrix} = \begin{pmatrix} E_{0x}e^{i\phi_x} \\ E_{0y}e^{i\phi_y} \\ 0 \end{pmatrix} e^{i(kz-\omega t)} \quad \text{(B.1)}$$

where $k = \omega/c$

The jones vector is defined as the vector $\begin{pmatrix} E_{0x}e^{i\phi_x} \\ E_{0y}e^{i\phi_y} \\ 0 \end{pmatrix}$, or simply

$$\begin{pmatrix} E_{0x}e^{i\phi_x} \\ E_{0y}e^{i\phi_y} \end{pmatrix} \quad \text{(B.2)}$$

Linearly polarized light occurs when the direction of the electric field remains constant, which means that the plane of polarization (defined by the electric field and the direction of propagation) is constant (or more precisely, parallel to the same plane).

Linearly polarized light at an angle θ with the x axis is described by the Jones vector

$$\begin{pmatrix} \cos\theta \\ \sin\theta \end{pmatrix} \quad \text{(B.3)}$$

as $\phi_x - \phi_y$ must be zero or an integer multiple of π.

Elliptically polarized light (with circular polarization being a special case) is generally described by the Jones vector

$$\begin{pmatrix} E_{0x} \\ E_{0y}e^{i\varepsilon} \end{pmatrix} \quad \text{(B.4)}$$

The field vector describes an ellipse on the transverse plane (i.e. the plane perpendicular to the direction of propagation). Special case of elliptically polarized light is circularly polarized (CP) light. Right hand CP light is described by the Jones vector $\frac{1}{\sqrt{2}}\begin{pmatrix} 1 \\ -i \end{pmatrix}$ and left hand CP light is described by the Jones vector $\frac{1}{\sqrt{2}}\begin{pmatrix} 1 \\ i \end{pmatrix}$.

Changes in the state of polarization can be achieved via several physical processes, such as reflection, scattering, refraction, and transmission.

As previously mentioned an optical element that transforms the polarization state into another is described by the Jones matrix acting on the incoming Jones vector:

$$\begin{bmatrix} E'_x \\ E'_x \end{bmatrix} = \begin{bmatrix} M_{11} & M_{12} \\ M_{21} & M_{22} \end{bmatrix} \begin{bmatrix} E_x \\ E_y \end{bmatrix} \quad \text{(B.5)}$$

Jones matrix for a polarizer

A linear polarizer does not affect the vibration direction of either E_x or E_y. This means that in (B.5) $M_{12} = M_{21} = 0$ and

$E'_x = p_x E_x \qquad 0 \leqslant p_x, p_y \leqslant 1$
$E'_y = p_y E_y$

So the Jones matrix is written as

$$J_p = \begin{bmatrix} p_x & 0 \\ 0 & p_y \end{bmatrix} \quad \text{(B.6)}$$

where we set $M_{11} = p_x$ and $M_{22} = p_y$

For an ideal horizontal polarizer, $J_p = \begin{bmatrix} 1 & 0 \\ 0 & 0 \end{bmatrix}$, while for an ideal vertical polarizer $J_p = \begin{bmatrix} 0 & 0 \\ 0 & 1 \end{bmatrix}$. For a non ideal polarizer both p_x and p_y have non zero values, but one is usually much smaller than the other.

When a linear polarizer is rotated by an angle θ then the Jones matrix needs to be accordingly rotated, using the rotation matrix, $R = \begin{bmatrix} \cos\,\theta & \sin\,\theta \\ -\sin\,\theta & \cos\,\theta \end{bmatrix}$, i.e.

$$J_p(\theta) = R^{-1} J_P R = \begin{bmatrix} \cos\,\theta & -\sin\,\theta \\ \sin\,\theta & \cos\,\theta \end{bmatrix} \begin{bmatrix} p_x & 0 \\ 0 & p_y \end{bmatrix} \begin{bmatrix} \cos\,\theta & \sin\,\theta \\ -\sin\,\theta & \cos\,\theta \end{bmatrix} =$$
$$\begin{bmatrix} p_x \cos^2\,\theta + p_y \sin^2\,\theta & (p_x - p_y)\sin\,\theta\cos\,\theta \\ -(p_x - p_y)\sin\,\theta\cos\,\theta & p_x \sin^2\,\theta + p_y \cos^2\,\theta \end{bmatrix} \quad \text{(B.7)}$$

For the ideal case, for a horizontal polarizer, $p_x = 1$ and $p_y = 0$ and hence the Jones matrix becomes $J_p(\theta) = \begin{bmatrix} \cos^2\,\theta & \sin\,\theta\cos\,\theta \\ -\sin\,\theta\cos\,\theta & \sin^2\,\theta \end{bmatrix}$ (B.8)

Polarization by reflection can be described by the Jones matrix of a non-ideal lineal polarizer.

Malus' law for an ideal and a real linear polarizer

Let as assume that the incident electric field is linearly polarized along the x axis, and can be described by the Jones vector $\begin{pmatrix} 1 \\ 0 \end{pmatrix}$. Then, according to (B.8) the resulting Jones vector will be given by $\begin{bmatrix} \cos^2\,\theta & \sin\,\theta\cos\,\theta \\ -\sin\,\theta\cos\,\theta & \sin^2\,\theta \end{bmatrix} \begin{pmatrix} 1 \\ 0 \end{pmatrix} = \begin{pmatrix} \cos^2\,\theta \\ -\sin\,\theta\cos\,\theta \end{pmatrix}$.

The amplitude of the emerging electric field will be therefore equal to $E_{0x}\cos\,\theta\sqrt{\cos^2\,\theta + \sin^2\,\theta} = E_{0x}\cos\,\theta$ = and hence the intensity of light ($\propto E^2$) will be given by

$$I = I_0 \cos^2\ \theta$$
(B.9)

which is Malus law for an ideal linear polarizer.

For a non-ideal polarizer, Malus law can be generalized using eq. (B.7) instead of (B.8), as follows:

$$\begin{bmatrix} E'_x \\ E'_y \end{bmatrix} = E_{0x} \begin{bmatrix} p_x \cos^2\ \theta + p_y \sin^2\ \theta & (p_x - p_y) sin\ \theta cos\ \theta \\ -(p_x - p_y) sin\ \theta cos\ \theta & p_x \sin^2\ \theta + p_y \cos^2\ \theta \end{bmatrix} \begin{pmatrix} 1 \\ 0 \end{pmatrix} =$$

$$= E_{0x} \begin{pmatrix} p_x \cos^2\ \theta + p_y \sin^2\ \theta \\ -(p_x - p_y) sin\ \theta cos\ \theta \end{pmatrix} \quad \text{(B.10)}$$

and $I = I_0 \left[\left(p_x\, cos^2\, \theta + p_y\, sin^2\, \theta \right)^2 + \left((p_x - p_y) sin\theta cos\theta \right)^2 \right] = I_0 [p_x{}^2 cos^4\theta +$
$p_y{}^2 sin^4\theta + 2p_x p_y cos^2\theta\ sin^2\theta + p_x{}^2 sin^2\theta\ cos^2\theta + p_y{}^2 sin^2\theta\ cos^2\theta -$
$2p_x p_y cos^2\theta\ sin^2\theta] \Rightarrow$

$$I = I_0 [p_x{}^2 cos^2\theta (\cos^2\theta + \sin^2\theta) + p_y{}^2 sin^2\theta (\cos^2\theta + \sin^2\theta)] \Rightarrow$$

$$I = I_0 [p_x{}^2 cos^2\theta + p_y{}^2 sin^2\theta] \quad \text{(B.11)}$$

This can also be re-written using the extinction ratio $R = p_y{}^2 / p_x{}^2$ (B.12) as

$I = I_0 p_x{}^2 [cos^2\theta + R sin^2\theta]$, which becomes identical to (B.9) for $p_x = 1,\ p_y = 0$

Malus law for a EUV reflective analyzer

Eq. (B.11) can be further generalized, if the polarizer (as is the case with the reflective analyzer used our experiment) also causes dephasing between the two components of the electric field.

In this case the Jones matrix can be written in the more general form

$$J_p = \begin{bmatrix} p_x e^{i\psi_x} & 0 \\ 0 & p_y e^{i\psi_y} \end{bmatrix}$$
(B.13)

We shall assume that the incident light is elliptically polarized as in (B.4) which can be equivalently written in the form $\begin{pmatrix} E_{0x} e^{i\varepsilon/2} \\ E_{0y} e^{-i\varepsilon/2} \end{pmatrix}$ (B.14)

Following the same methodology, we can write for the emerging field:

$$\begin{bmatrix} E'_x \\ E'_y \end{bmatrix} = \begin{bmatrix} p_x e^{i\psi_x} \cos^2\ \theta + p_y e^{i\psi_y} \sin^2\ \theta & \left(p_x e^{i\psi_x} - p_y e^{i\psi_y} \right) sin\ \theta cos\ \theta \\ -\left(p_x e^{i\psi_x} - p_y e^{i\psi_y} \right) sin\ \theta cos\ \theta & p_x e^{i\psi_x} \sin^2\ \theta + p_y e^{i\psi_y} \cos^2\ \theta \end{bmatrix} \begin{pmatrix} E_{0x} e^{i\varepsilon/2} \\ E_{0y} e^{-i\varepsilon/2} \end{pmatrix}$$

The intensity is then proportional to

$I(\theta, \varepsilon) \propto E'^2_x \ + \ E'^2_y \ =$

$= {p_x}^2\left[E^2_{0x}(cos^2\ \theta + Rsin^2\ \theta) + E^2_{0y}(Rcos^2\theta + sin^2\theta) + E_{0x}E_{0y}(R-1)sin2\theta\ cos\varepsilon\right]$ (B.15), where R is given by (B.12) (cf Skantzakis et al. 2016).

One can use (B.15) to derive the ratio E_{0y}/E_{0x} for the incident light, from the measured distribution of intensity as a function of θ, by noting the values of I at $\theta = 0$ (I_1) and $\theta = \pi/2$ (I_2):

$$I_1 \propto {p_x}^2\left[E^2_{0x} + E^2_{0y}\mathrm{R}\right] \quad \text{(B.16)}$$

$$I_2 \propto {p_x}^2\left[E^2_{0x}R + E^2_{0y}\right] \quad \text{(B.17)}$$

From eq. (B.16) and (B.17) we get that

$$\frac{I_1}{I_2} = \frac{E^2_{0x}+E^2_{0y}\mathrm{R}}{RE^2_{0x}+E^2_{0y}} = \frac{\beta+\mathrm{R}}{R\beta+1} \quad \text{(B.18)}$$

where $\beta = \frac{E^2_{0x}}{E^2_{0y}}$

So

$\frac{E^2_{0x}}{E^2_{0y}} = \frac{R-c}{cR-1}$, with $c \equiv contrast = \frac{I_1}{I_2}$

and

$$\frac{E_{0x}}{E_{0y}} = \sqrt{\frac{R-c}{cR-1}} \quad \text{(B.19)}$$

Bibliography:

Damian, I., 2004, Buletinul Stiintific al Universitatii Politehnica din Timisoara, tom 49(63), 2, p. 107, Matematica-Fizica, arXiv:physics/0604073 [physics.ed-ph]

Papazoglou, D., 2021, "Wave Optics and Optical Metrology, MSc course, notes

Skantzakis, E., Chatziathanasiou, S., Carpeggiani, P. *et al.* Polarization shaping of high-order harmonics in laser-aligned molecules. *Sci Rep* **6,** 39295 (2016).

Appendix C

Python script used for the data reduction and calibration

```
#%%
import matplotlib.pyplot as plt
import numpy as np
#%%
path=r'C:/Μεταπτυχιακό/διπλωματικη/Αναλυση δεδομενων/2610/26-10-2021
circular harmonics (2) 399nm step1 no Sn Ar Ar.txt'
Data=np.loadtxt(fname=path,usecols=(0,1),skiprows=5)
Data[:,1]=np.abs(Data[:,1])
#%%
# list_time=Data[:,0]
new_listtime=Data[:,0]
list_intensity=Data[:,1]
plt.figure(2)
plt.plot(new_listtime, list_intensity)
plt.xlabel('Time ')
plt.ylabel('Intensity')
plt.grid()
plt.legend()
plt.show()
#%%
new_listtime=Data[:,0] + 2.368*10**(-7)
# newnew_listtime= [item for item in new_listtime if item>=0]
keepvals=(new_listtime>0)
list_intensity=Data[:,1]
plt.plot(new_listtime[keepvals], list_intensity[keepvals])
plt.xlabel('Time ')
plt.ylabel('Intensity')
plt.grid()
plt.legend()
plt.show()
#%%
#def multiply(a):
  #  return (1/a**2)
# newnew_listtime = list(map(multiply,keepvals))
revtime=new_listtime[keepvals]**(-2)
list_intensity=Data[:,1]
plt.plot(revtime,list_intensity[keepvals])
# plt.plot(newnew_listtime,list_intensity[keepvals])
plt.xlabel('1/Timesquare')
plt.ylabel('Intensity')
plt.xlim(10**(10),10**(14))
plt.grid()
plt.legend()
plt.show()
```

```
#%%
# def multiply(a):
#     return (1/a)*(1/a)
# newnew_listtime = list(map(multiply,new_listtime[keepvals]))
# #revtime=new_listtime[keepvals]**(-2)
# list_intensity=Data[:,1]
# from scipy.signal import find_peaks
# peaks = find_peaks(list_intensity, height = 1, threshold = 1, distance = 1)
# height = peaks[1]['peak_heights'] #list of the heights of the peaks
# peak_pos = newnew_listtime[peaks[0]] #list of the peaks position
# plt.plot(newnew_listtime,list_intensity[keepvals])
# plt.xlabel('1/Timesquare')
# plt.ylabel('Intensity')
# plt.xlim(10**(10),2*10**(14))
# plt.grid()
# plt.legend()
# plt.show()
#%%
x=[4.919*10**12,1.317*10**13,1.7355*10**13,2.5792*10**13,3.005*10**13]
E=[17.05,20.15,21.7,24.8,26.35]
m,b = np.polyfit(x, E, 1)
plt.plot(x,'.')
plt.xlabel('newtime')
plt.ylabel('HarmonicsEnergy')
plt.grid()
plt.legend()
plt.show()
#%%
#x=np.array([1.483*10**13,2.366*10**13,3.24578*10**13,4.133*10**13,5.00669*
10**13])
#E=np.array([17.05,20.15,23.25,26.35,29.45])
#fit = np.polyfit(x, E, 2)
#a = fit[0]
#b = fit[1]
#c = fit[2]
#fit_equation = a *np.square(x) + b*x + c
#Plotting
#fig1 = plt.figure()
#ax1 = fig1.subplots()
#ax1.plot(x, fit_equation,color = 'r',alpha = 0.5, label = 'Polynomial fit')
#ax1.scatter(x, E, s = 5, color = 'b', label = 'Data points')
#ax1.set_title('Polynomial fit example')
#ax1.legend()
#plt.show()
#%%
def Energy(c):
   return (3.6984449381267416e-13)*c +  15.25767510756325
```

```
newEnergy = list(map(Energy,revtime))
def transformationfunction(d):
  return (d/(15.25767510756325))
newintensity = list(map(transformationfunction,list_intensity[keepvals]))
plt.plot(newEnergy,newintensity)
plt.xlim(15,30)
# plt.ylim(0,10000)
plt.xlabel('Energy')
plt.ylabel('Intensity')
plt.grid()
plt.legend()
plt.show()
#%%
a = np.array([newEnergy,newintensity])
data = np.column_stack([newEnergy, newintensity])
mat = np.matrix(a)
np.savetxt('C:/Μεταπτυχιακό/διπλωματικη/Αναλυση δεδομενων/2510-1/7.txt',
data, delimiter=',')
#%%
a=newEnergy
b=newintensity
c = [a, b]
with open("listlinear2.txt", "w") as file:
   for x in zip(*c):
      file.write("{0}\t{1}\n".format(*x))
```

Appendix D

Same as Figures 10-14 but with $E_{2\omega}$ instead of $\lambda_{2\omega}$ for the horizontal axis.

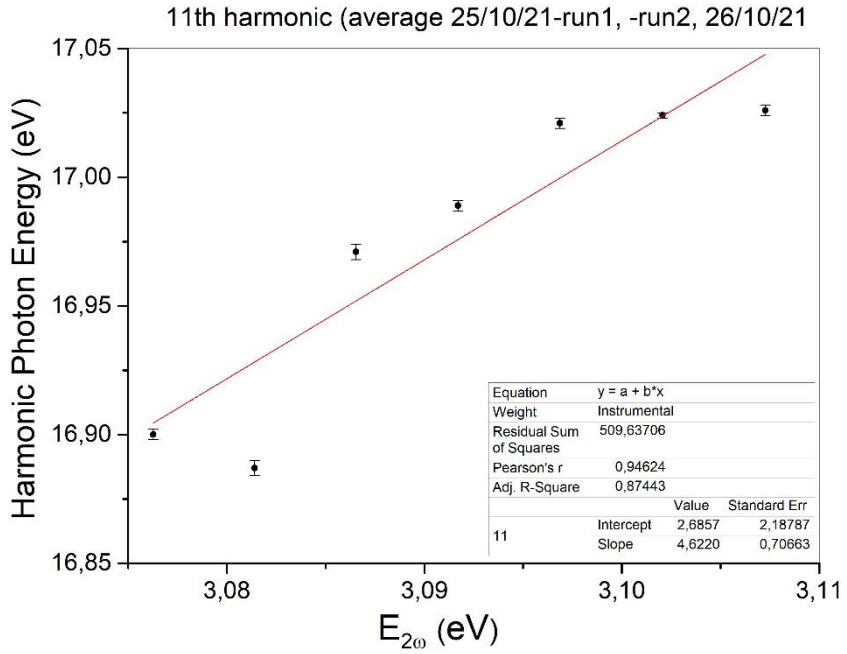

Figure 10a: *Energy (three run average) of the 11th harmonic as a function of* $E_{2\omega}$ (eV).

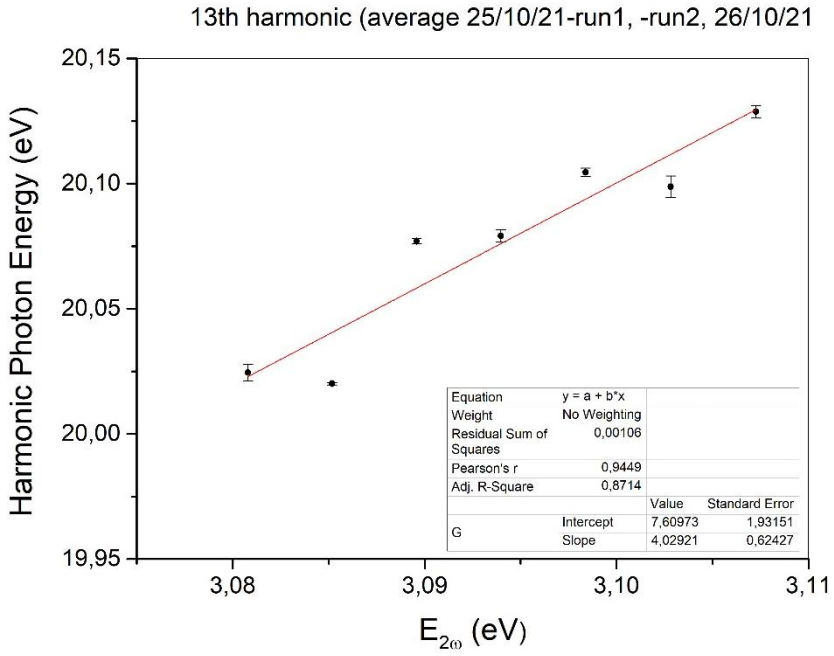

Figure 11a: *Energy (three run average) of the 13th harmonic as a function of* $E_{2\omega}$ (eV).

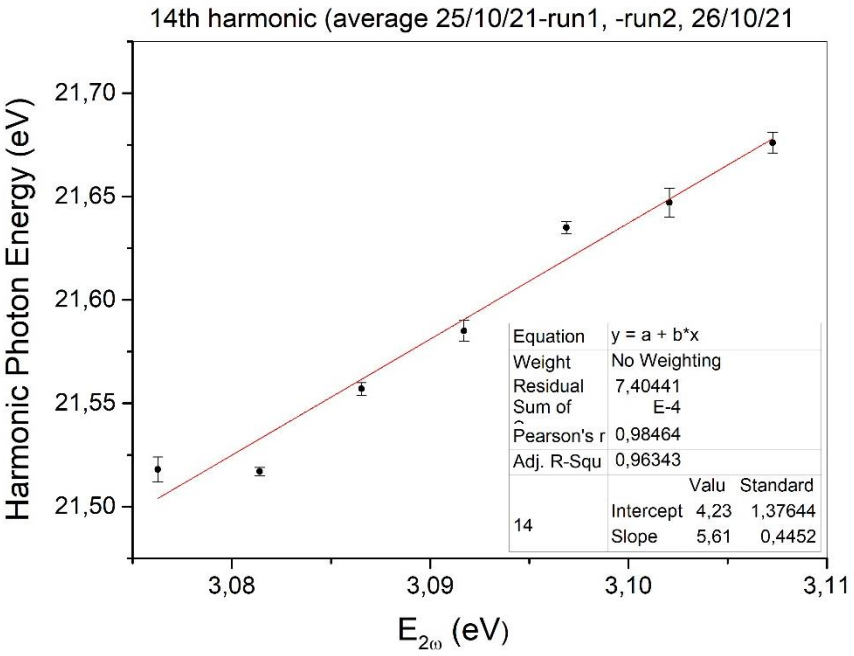

Figure 12a: *Energy (three run average) of the 14th harmonic as a function of $E_{2\omega}$* (eV).

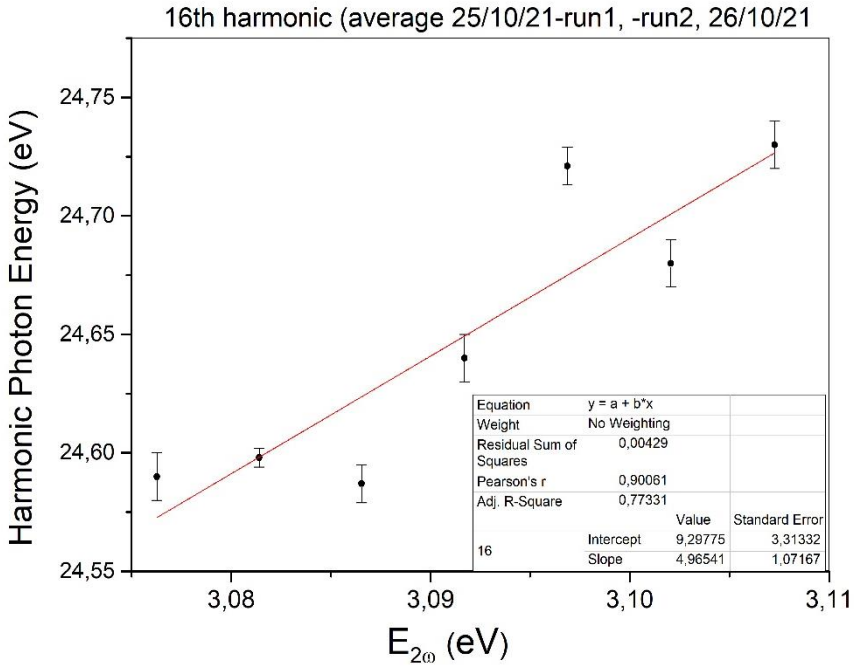

Figure 13a: *Energy (three-run average) of the 16th harmonic as a function of $E_{2\omega}$ (eV).*

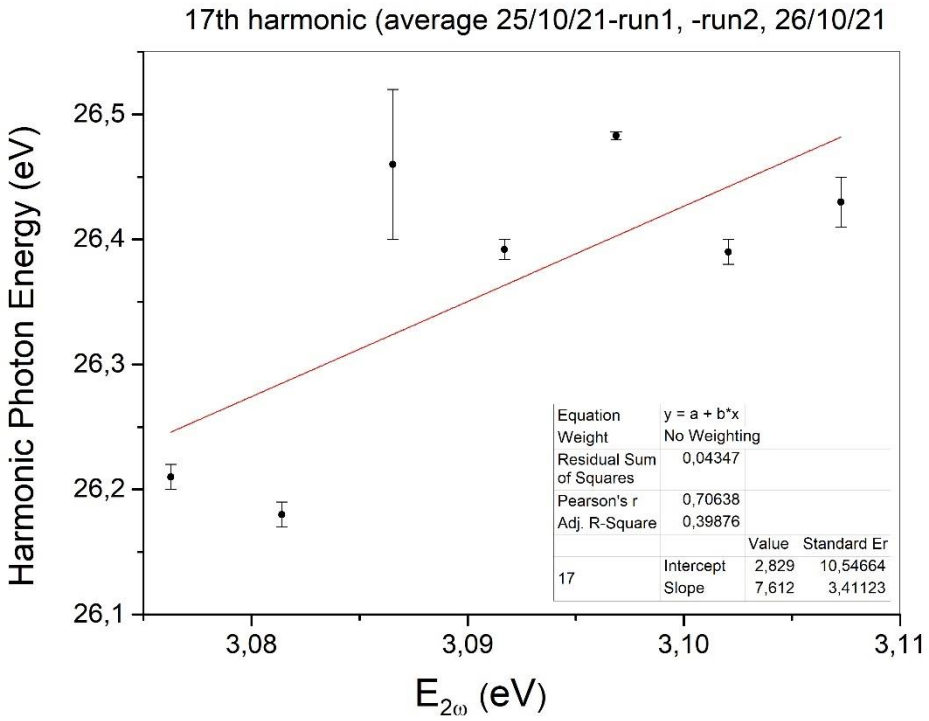

Figure 14a: *Energy (three run average) of the 17th harmonic as a function of $E_{2\omega}$ (eV)*